



Large-scale rigid-body rotation in the mantle wedge and its implications for seismic tomography

Weronika Gorczyk

Geological Institute, Swiss Federal Institute of Technology (ETH - Zürich), LEB, Leonhaedstrasse 19, CH8092 Zurich, Switzerland (weronika.gorczyk@erdw.ethz.ch)

Taras V. Gerya

Geophysical Institute, Swiss Federal Institute of Technology (ETH - Zürich), ETH Hoenggerberg, HPP, CH8093 Zurich, Switzerland

Institute of Experimental Mineralogy, Russian Academy of Sciences, 142432 Chernogolovka, Moscow, Russia

James A. D. Connolly

Geological Institute, Swiss Federal Institute of Technology (ETH - Zürich), Sonneggstrasse 5, CH8092 Zurich, Switzerland

David A. Yuen

Department of Geology and Geophysics, University of Minnesota, Minneapolis, Minnesota 55455-0219, USA

Maxwell Rudolph

Department of Geology, Oberlin College, Oberlin, Ohio, 44074, USA

[1] Using a combined finite difference and marker-in-cell technique, we performed two-dimensional coupled petrological-thermomechanical numerical simulations of intraoceanic subduction. The simulations indicate that parts of the mantle wedge can become trapped between rheologically weak, hydrated, and partially molten upwellings (cold plumes) and the subducting slab. The structures form at various depths and develop circular, elliptic, or irregular shapes. The combined effect of the tractions caused by upwelling and subduction causes these regions to rotate. Our simulations investigate the parameters controlling the occurrence and long-term stability of such rigid, rotating structures. Circular rotating structures like “subduction wheels” are characteristic of models with relatively young (20–30 Myr) slabs and intermediate (2–5 cm/yr) subduction rates. We propose that the development of such circular features may explain some of the isolated seismic velocity anomalies in the mantle wedge.

Components: 10,480 words, 14 figures, 5 tables, 6 animations.

Keywords: subduction zone; mantle plume; arc extension; seismic tomography; 2-D numerical modeling.

Index Terms: 8033 Structural Geology: Rheology: mantle (8162); 8121 Tectonophysics: Dynamics: convection currents, and mantle plumes.

Received 15 July 2005; **Revised** 29 November 2005; **Accepted** 15 February 2006; **Published** 23 May 2006.

Gorczyk, W., T. V. Gerya, J. A. D. Connolly, D. A. Yuen, and M. Rudolph (2006), Large-scale rigid-body rotation in the mantle wedge and its implications for seismic tomography, *Geochem. Geophys. Geosyst.*, 7, Q05018, doi:10.1029/2005GC001075.

1. Introduction

[2] Understanding the dynamic mechanisms driving various processes within subduction zones has been the focus of many recent seismic tomography studies [e.g., *Deal and Nolet*, 1999; *Wortel and Spakman*, 2000], and geodynamic modeling efforts [e.g., *Ponko and Peacock*, 1995; *van Hunen et al.*, 2000; *Regenauer-Lieb et al.*, 2001; *Honda et al.*, 2002; *Honda and Saito*, 2003; *Billen and Gurnis*, 2001; *Gerya and Yuen*, 2003a; *Manea et al.*, 2005]. Seismic structures with both positive and negative velocity anomalies are found beneath volcanic arcs near trenches [e.g., *Zhao*, 2004; *Zhang et al.*, 2004; *van der Meijde et al.*, 2005]. Additionally, strong isometric isolated positive V_p attenuation anomalies enveloped within a region characterized by a negative V_p attenuation anomaly have been observed above the descending slab [e.g., *Schurr et al.*, 2003]. These structures are interpreted as thermal [*Tamura et al.*, 2002] or chemical [*Gerya and Yuen*, 2003a] anomalies, but the distribution and evolution of these anomalies is not fully understood.

[3] *Gerya and Yuen* [2003a] investigated the propagation of partially molten diapiric structures (“cold plumes”) into the mantle wedge above a slab. They concluded that cold plumes are driven by Rayleigh-Taylor instabilities that develop at the top of subducting slab. Diapirs rise through the mantle wedge along trajectories determined by the balance between buoyancy forces and mantle flow [*Stern*, 2002; *Manea et al.*, 2005]. It was determined that both positive and negative seismic velocity anomalies are associated with the plumes [*Gerya et al.*, 2006]. Positive anomalies are prevalent close to the slab due to the lowered temperatures associated with regions of cold plume initiation. Strong negative seismic anomalies develop at shallower depth due to the partially molten rocks that form plume heads. However, existence of isolated isometric positive tomographic anomalies surrounded by negative anomalies was not explained. Therefore we explore *Gerya and Yuen*’s [2003a] model extended by accounting for the dynamic behavior of slab dehydration and variation in density of subducted rocks [*Gerya et al.*, 2006]. We calculate phase changes and rock properties for the model lithologies by Gibbs energy minimization [*Connolly*, 2005]. Calculated rock properties, such as density, heat capacity, thermal expansivity and water content feed back [*Gerya et al.*, 2004b; *Vasilyev et al.*, 2004] on the geodynamic evolution of the subduction zone. With this approach we investigate development of hydrated mantle and partially molten cold plumes above the slab at multiple scales (Appendix A). The

models show that generation of rigid, rotating bodies within the mantle wedge is a natural consequence of plume formation. We hypothesize that such bodies may explain the existence of the aforementioned isolated positive tomographic anomalies in upper mantle wedges.

2. Petrological and Thermomechanical Model

[4] We use the modified thermomechanical I2VIS code, which uses a nondiffusive marker-in-cell technique [*Gerya and Yuen*, 2003b; *Gerya et al.*, 2004a]. The initial thermomechanical setup is based on a 2-D subduction model (Figure B1 in Appendix B). The rate of subduction is prescribed along whole length of bending subducting slab with the variable angle of subduction changing from 0 to 45 degrees. The boundary conditions account for horizontal flow in the asthenosphere under the over-riding plate. The code has been modified [*Gerya et al.*, 2004b; *Vasiliev et al.*, 2004] to incorporate a coupled petrological and seismic velocity model [*Gerya et al.*, 2006]. The lithological configuration is described in Table B1 in Appendix B. In this approach, we calculate the stable mineralogy and thermodynamic properties for each lithology as a function of pressure and temperature by Gibbs energy minimization [*Connolly*, 2005]. The phase relations obtained by such calculations for lithologies relevant here have been presented elsewhere [*Kerrick and Connolly*, 1998, 2001a, 2001b]. Seismic velocities were computed as described by *Connolly and Kerrick* [2002] with shear moduli as summarized by *Connolly* [2005]. All rock properties, including effective density, isobaric heat capacity, thermal expansion, latent heating and water content are calculated for each marker at every time step. We solved the momentum, continuity, and temperature equations for the two-dimensional creeping-flow approximation by using finite difference method. We account for thermal and chemical buoyancy along with radioactive, shear, adiabatic and latent heating. The model has been validated through a series of test cases [*Gerya and Yuen*, 2003b] and its results are consistent with a variety of geological data [e.g., *Gerya et al.*, 2002; *Willner et al.*, 2002, 2004]. Detailed description of the model is available in Appendix B.

[5] We have gathered results from 103 numerical experiments (see Table 1 for selected runs; a remaining runs description is available in Table 2). These simulations have been calculated over a finite difference grid with 201×101 to 201×401 regularly

Table 1. Grid Step: 2 km-201 × 101 Nodes, ~0.5 Million Markers^a

Model	Slab Rate, cm/yr	Slab Age, Myr	η_{serp} , Pa s	Eros., Sedim. Rate, mm/yr	Plumes Initiation			Rigid Body Rotation		
					Time, Myr	Depth, km	Rocks	Fore-Arc Spins	Subduction Wheel	Wedge Pinball
1. (02_18_02) ^b	2	20	10 ¹⁸	0.3	10–45	62–150	p, c ≪ p, c ≈ p			x
2. (02_18_02H)	2	20	10 ¹⁸	0.3	11–81	62–194	p, c ≪ p, c + p, c ≈ p			x
3. (02_18_03) ^b	3	20	10 ¹⁸	0.3	5–45	63–160	p, c ≪ p, c + p			
4. (02_18_03H)	3	20	10 ¹⁸	0.3	9–85	80–190	p, c ≪ p, c ≈ p			x
5. (02_18_04) ^b	4	20	10 ¹⁸	0.3	4–34	65–70	p, c ≈ p			x
6. (02_18_04H)	4	20	10 ¹⁸	0.3	5–47	65–278	p, c ≪ p, c ≈ p			x
7. (02_18_05) ^b	5	20	10 ¹⁸	0.3	3–27	69–90	p, c ≪ p, c ≈ p			x
8. (02_18_05H)	5	20	10 ¹⁸	0.3	4–27	50–122	p, c ≪ p, c ≈ p			x
9. (02_18_06H)	6	20	10 ¹⁸	0.3	2–15	52–70	p, c ≪ p			
10. (02_19_01) ^b	1	20	10 ¹⁹	0.3	33	70	c			
11. (02_19_01H)	1	20	10 ¹⁹	0.3	3–11	48–87	c ≈ p, c			
12. (02_19_02) ^b	2	20	10 ¹⁹	0.3	11–97	67–112	p, c ≪ p, c ≈ p, c ≫ p			x
13. (02_19_02H)	2	20	10 ¹⁹	0.3	6–93	52–200	p, c ≪ p, c ≈ p			x
14. (02_19_03) ^b	3	20	10 ¹⁹	0.3	5–64	65–119	p, c ≪ p, c + p, c ≈ p			x
15. (02_19_03H)	3	20	10 ¹⁹	0.3	4–94	50–200	p, c ≪ p, c ≈ p			
16. (02_19_04) ^b	4	20	10 ¹⁹	0.3	4–47	76–130	p, c ≪ p, c ≈ p			x
17. (02_19_04H)	4	20	10 ¹⁹	0.3	3–53	50–170	p, c ≪ p, c ≈ p			x
18. (02_19_05) ^b	5	20	10 ¹⁹	0.3	3–21	70–90	p, c ≪ p, c ≈ p			x
19. (02_19_05H)	5	20	10 ¹⁹	0.3	24–131	70–149	c ≈ p, c			
20. (02_19_06H)	6	20	10 ¹⁹	0.3	2–8	60–124	p			
21. (03_18_01H)	1	30	10 ¹⁸	0.3	21–110	92–180	p, c ≪ p			
22. (03_18_02H)	2	30	10 ¹⁸	0.3	6–89	62–185	p, c ≪ p, c ≈ p			x
23. (03_18_03H)	3	30	10 ¹⁸	0.3	6–52	58–200	p, c ≪ p			
24. (03_19_02H)	2	30	10 ¹⁹	0.3	9–136	65–193	p, c ≪ p, c ≈ p			x
25. HIGH ^c	2	40	10 ¹⁹	0.3	4–48	58–90	p, c + p			x
26. (06_19_02) ^b	2	60	10 ¹⁹	0.3 0.6	9–50	87–110	p, c + p p, c ≪ p, c + p			
					9–52	80–194				
27. (08_19_02) ^b	2	80	10 ¹⁹	0.3 0.6	9–32	92–160	p, c ≈ p p, c + p			
					8–31	82–185				
28. (10_19_02) ^b	2	100	10 ¹⁹	0.3	9–35	92–195	p			
29. (10_18_04H)	4	100	10 ¹⁸	0.3	59–63	81–97	c + p			x
30. (10_18_05) ^b	5	100	10 ¹⁸	0.3	2	80	p			
31. (10_18_05H)	5	100	10 ¹⁸	0.3	30–50	60–200	p			x
32. (10_19_04) ^b	4	100	10 ¹⁹	0.3	3–8	85–197	p			
33. (10_19_04H)	4	100	10 ¹⁹	0.3	50–73	60–155	p, c + p			x
34. (10_19_05) ^b	5	100	10 ¹⁹	0.3	2	82	p			x
35. (10_19_05H)	5	100	10 ¹⁹	0.3	25–63	50–190	p			x

^aRock abbreviations: P, peridotite; c, subducted crustal rocks (sediments, oceanic crust).

^bSimplified hydration model [Gerya and Yuen, 2003a]: subducted oceanic crust dehydration – $v_{h(x)} = 0.05v_{\text{subd}}$ when $0 < x < x_A$; serpentine dehydration in the slab $v_{h(x)} = Kv_{\text{subd}}$, when $x_A < x < x_B$; no deep dehydration of the slab – $v_{h(x)} = 0$ when $x > x_B$, where $v_{h(x)}$ is the substantive hydration rate along the hydration front (equation (B3)) as the function of horizontal distance x , x_A and x_B are imposed limits for the interval of serpentine dehydration in the slab (Table B3), K is mantle hydration constant (K = 0.5 for the mantle below wet solidus, K = 0.15 for the mantle above wet solidus).

^cGrid step: 1 km–401 × 201 nodes, ~10 million markers.

spaced Eulerian points, using 0.5 million to 10 billion markers (Appendix A). In the course of monitoring so many runs and studying the various effects, the importance of visualization became quite obvious and we had to develop some new techniques of looking at large data sets, these are described in the Appendix A.

3. Results of Simulations

[6] Cold plume development is enhanced by the dehydration of the subducting slab. As a result of

dehydration of descending slab, aqueous fluids migrate and hydrate the mantle wedge near the slab [e.g., Gerya et al., 2002]. Due to dynamics of the hydration front, Rayleigh-Taylor instabilities can develop above the subducting slab. These instabilities develop at the depth range of 60–100 km and trigger the upward migration of partially molten upwellings that are 300–400 degrees colder than surrounding mantle [Tamura, 1994; Gerya and Yuen, 2003a]. The evolution of cold plumes varies with different sets of initial conditions such as subduction rate, slab age, mantle viscosity, and

Table 2. Results of Simulations That Were Not Included in Table 1^a

Model	Slab Rate, am/yr	Slab Age, Myr	η_{serp} , Pa s	Eros., Sedim. Rate, mm/yr	Plumes Initiation		
					Time, Myr	Depth, km	Rocks
(02_18_01) ^b	1	20	10 ¹⁸	0.3	27	80	c
(02_18_01H)	1	20	10 ¹⁸	0.3	42	65	c ≫ p
(03_18_04H)	4	30	10 ¹⁸	0.3	3–51	71–167	p, c ≪ p
(03_18_05H)	5	30	10 ¹⁸	0.3	4–61	52–83	p
(03_19_01H)	1	30	10 ¹⁹	0.3	38–227	110–150	c ≪ p, c ≈ p
(03_19_03H)	3	30	10 ¹⁹	0.3	4–63	83–178	p, c ≪ p
(03_19_04H)	4	30	10 ¹⁹	0.3	2–33	67–85	p
(03_19_05H)	5	30	10 ¹⁹	0.3	3–19	65–93	p
(04_18_01) ^b	1	40	10 ¹⁸	0.3	34–94	92–200	p, c ≈ p
(04_18_01H)	1	40	10 ¹⁸	0.3	18–100	65–188	p, c ≪ p, c + p
(04_18_02) ^b	2	40	10 ¹⁸	0.3	9–44	77–195	p, c ≪ p, c ≪ p, c ≈ p
(04_18_02H)	2	40	10 ¹⁸	0.3	9–45	78–178	p, c ≪ p, c + p
(04_18_03) ^b	3	40	10 ¹⁸	0.3	5–39	81–100	p, c ≪ p, c + p, c ≈ p
(04_18_03H)	3	40	10 ¹⁸	0.3	5–37	70–190	p, c + p, c ≈ p
(04_18_04) ^b	4	40	10 ¹⁸	0.3	4–15	81–180	p, c ≪ p, c ≈ p, c ≫ p
(04_18_04H)	4	40	10 ¹⁸	0.3	3–13	58–190	p, c + p
(04_18_05) ^b	5	40	10 ¹⁸	0.3	3–20	79–122	p
(04_18_05H)	5	40	10 ¹⁸	0.3	2–14	59–119	p, c ≪ p, c + p, c ≈ p
(04_19_01H)	1	40	10 ¹⁹	0.3	19–100	80–198	p, c + p, c ≈ p
(04_19_02H)	2	40	10 ¹⁹	0.3 0.6	9–52	77–192	p, c ≪ p, c ≈ p p, c ≪ p
					9–146	59–200	
(04_19_03H)	3	40	10 ¹⁹	0.3 1	5–36	92–180	p, c ≪ p, c ≈ p p
					8–52	57–197	
(04_19_04H)	4	40	10 ¹⁹	0.3 1.3	3–27	55–178	p, c ≪ p, c ≈ p p, c ≪ p
					2–50	57–198	
(04_19_05H)	5	40	10 ¹⁹	0.3 1.6	2–12	57–116	p, c ≪ p p, c ≪ p c + p
					2–27	49–140	
(06_18_01) ^b	1	60	10 ¹⁸	0.3	26–101	107–180	p, c ≪ p, c ≈ p, c ≫ p
(06_18_01H)	1	60	10 ¹⁸	0.3	20–108	81–180	p, c ≪ p, c ≈ p
(06_18_02) ^b	2	60	10 ¹⁸	0.3	9–30	87–102	p, c ≪ p, c + p, c ≈ p
(06_18_02H)	2	60	10 ¹⁸	0.3	10–119	82–200	c ≪ p, c + p
(06_18_03) ^b	3	60	10 ¹⁸	0.3	5–9	83–175	p
(06_18_03H)	3	60	10 ¹⁸	0.3	5–65	100–200	P
(06_18_04) ^b	4	60	10 ¹⁸	0.3	4–7	78–172	p, c ≪ p
(06_18_04H)	4	60	10 ¹⁸	0.3	3–7	95–194	p, c ≪ p
(06_18_05) ^b	5	60	10 ¹⁸	0.3	3	80	p, c ≪ p
(06_18_05H)	5	60	10 ¹⁸	0.3	3–6	107–196	p, c ≪ p
(06_19_01) ^b	1	60	10 ¹⁹	0.3	35–84	117–175	p, c ≪ p, c ≫ p, c
(06_19_01H)	1	60	10 ¹⁹	0.3	20–135	76–200	p, c ≪ p
(06_19_02H)	2	60	10 ¹⁹	0.3	11–112	57–200	p, c ≪ p
(06_19_03) ^b	3	60	10 ¹⁹	0.31	9–25	90–112	p p, c ≪ p, c + p
					9–25	87–183	
(06_19_03H)	3	60	10 ¹⁹	0.3	5–9	63–193	p
(06_19_04) ^b	4	60	10 ¹⁹	0.3 1.3	3–24	80–176	p p, c + p
					9–25	87–189	
(06_19_04H)	4	60	10 ¹⁹	0.3	3–15	84–175	p
(06_19_05) ^b	5	60	10 ¹⁹	0.3 1.6	3–82	78–112	p, c ≪ p p, c + p, c ≫ p
					9–63	81–179	
(06_19_05H)	5	60	10 ¹⁹	0.3	62	100	p
(08_18_01) ^b	1	80	10 ¹⁸	0.3	35–73	118–200	p
(08_18_01H)	1	80	10 ¹⁸	0.3	20–84	78–194	p, c ≪ p
(08_18_02) ^b	2	80	10 ¹⁸	0.3	8–15	88–180	p, c ≪ p, c + p
(08_18_02H)	2	80	10 ¹⁸	0.3	30–70	91–183	p, c ≪ p
(08_18_03) ^b	3	80	10 ¹⁸	0.3	5–10	83–162	p
(08_18_03H)	3	80	10 ¹⁸	0.3 1	85 4–15	120 95–160	p p
(08_18_04) ^b	4	80	10 ¹⁸	0.3	3–8	78–192	p
(08_18_04H)	4	80	10 ¹⁸	0.3	5	117	p
(08_18_05) ^b	5	80	10 ¹⁸	0.3	3–7	78–197	p
(08_18_05H)	5	80	10 ¹⁸	0.3	4	119	p
(08_19_01) ^b	1	80	10 ¹⁹	0.3	40–74	98–200	p, c ≈ p, c ≫ p

Table 2. (continued)

Model	Slab Rate, am/yr	Slab Age, Myr	η_{serp} , Pa s	Eros., Sedim. Rate, mm/yr	Plumes Initiation		
					Time, Myr	Depth, km	Rocks
(08_19_04) ^b	4	80	10^{19}	0.3 1.3	3–9 4–7	81–157 81–197	p p
(08_19_05) ^b	5	80	10^{19}	0.3 1.6	3 3	79 78	p p
(10_18_01) ^b	1	100	10^{18}	0.3	40–60	118–182	p, c \ll p
(10_18_01H)	1	100	10^{18}	0.3	-	-	-
(10_18_02) ^b	2	100	10^{18}	0.3	8–30	90–100	p, c \ll p, c + p
(10_18_02H)	2	100	10^{18}	0.3	-	-	-
(10_18_03) ^b	3	100	10^{18}	0.3	5–9	85–137	p
(10_18_03H)	3	100	10^{18}	0.3	101–108	117–140	p, c + p
(10_18_04) ^b	4	100	10^{18}	0.3	3–7	82–180	p
(10_19_01) ^b	1	100	10^{19}	0.3	9–57	100–120	p, c \approx p, c \gg p, c
(10_19_01H)	1	100	10^{19}	0.3	-	-	-
(10_19_02H)	2	100	10^{19}	0.3	-	-	-
(10_19_03) ^b	3	100	10^{19}	0.3	5	92	p
(10_19_03H)	3	100	10^{19}	0.3	-	-	-

^aAll runs with rigid body rotation are shown within Table 1. Grid step: 2 km – 201 × 101 nodes, ~0.5 million markers. Rock abbreviations: p, peridotite; c, subducted crustal rocks (sediments, oceanic crust).

^bSimplified hydration model [Gerya and Yuen, 2003a]: subducted oceanic crust dehydration – $v_{h(x)} = 0.05v_{\text{subd}}$ when $0 < x < x_A$; serpentine dehydration in the slab $v_{h(x)} = Kv_{\text{subd}}$, when $x_A < x < x_B$; no deep dehydration of the slab – $v_{h(x)} = 0$ when $x > x_B$, where $v_{h(x)}$ is the substantive hydration rate along the hydration front (equation (B3)) as the function of horizontal distance x , x_A and x_B are imposed limits for the interval of serpentine dehydration in the slab (Figure B1, Table B3), K is mantle hydration constant ($K = 0.5$ for the mantle below wet solidus, $K = 0.15$ for the mantle above wet solidus).

intensity of the erosion/sedimentation process. Yet the evolution of rigid body rotation is controlled mostly by the subduction rate and slab age, and is strongly associated with cold plume development. Systematic study [Gerya *et al.*, 2006] shows that two distinct types of plumes form in the mantle wedge (Table 1): (1) mixed, which consist of both crustal and mantle rocks, and (2) unmixed, composed of partially molten hydrated peridotite. Propagation of plumes introduces strong rheological non-homogeneity into the mantle wedge since hydrated partially molten rocks composing plumes are characterized by much lower viscosity ($<10^{17}$ Pa · s) than the surrounding dry mantle (10^{18} – 10^{21} Pa · s). Under conditions of intense mantle flow in the wedge its rheological non-homogeneity results in spontaneous isolation of various rigid objects described in the following sections. Such phenomena only appear in numerical experiments accounting for the hydration and melting above slabs [Gerya and Yuen, 2003b] and they cannot be observed within the models which have far less physical and chemical complexities [Peacock *et al.*, 2005].

3.1. Subduction Wheel

[7] For experiments with relatively warm slabs, corresponding to slab ages of ~20–30 Myr, intense slab dehydration occurs at depths of 60–70 km. Therefore plume initiation for these slabs occurs at

shallow depth. Plume development may lead to the isolation of non-hydrated mantle fragments of 35–50 km in diameter between the plume root, plume head, and descending slab. At the time of isolation the body has the same viscosity and temperature as the ambient mantle. If the plume root remains stable for sufficient time (~20 Myr), strong vorticity develops in the displacement field within the corner of the asthenospheric portion of the mantle wedge close to the slab (Figure 2). The isolated area begins to rotate and becomes rounded due to the moment between subducting slab and rising plume. The body is enveloped by 5–8 km of plume material, which separates it from the mantle wedge. The plume material is less viscous ($<10^{17}$ Pa · s) than its surroundings due to hydration and the presence of melts. This phenomenon, designated a “subduction wheel,” is depicted in Figures 1, 2, 3 and 4. With time the body cools (by 200–300°C) and consequently its viscosity becomes much higher, up to 10^{22} – 10^{24} Pa · s (Figure 3). The seismic velocity anomaly within this body notably (by 2%) increases (Figure 2). After the increase in viscosity, the rigid object becomes unstable and detaches from the root. Then, the wheel migrates by either descending with the slab (Figures 1 and 2) or moves near-horizontally into the hotter portion of the mantle wedge (Figures 3 and 4) where it subsequently vanishes. Migration of the wheel is caused by episodic subduction of large amounts of material from the serpentinized channel pushing the wheel

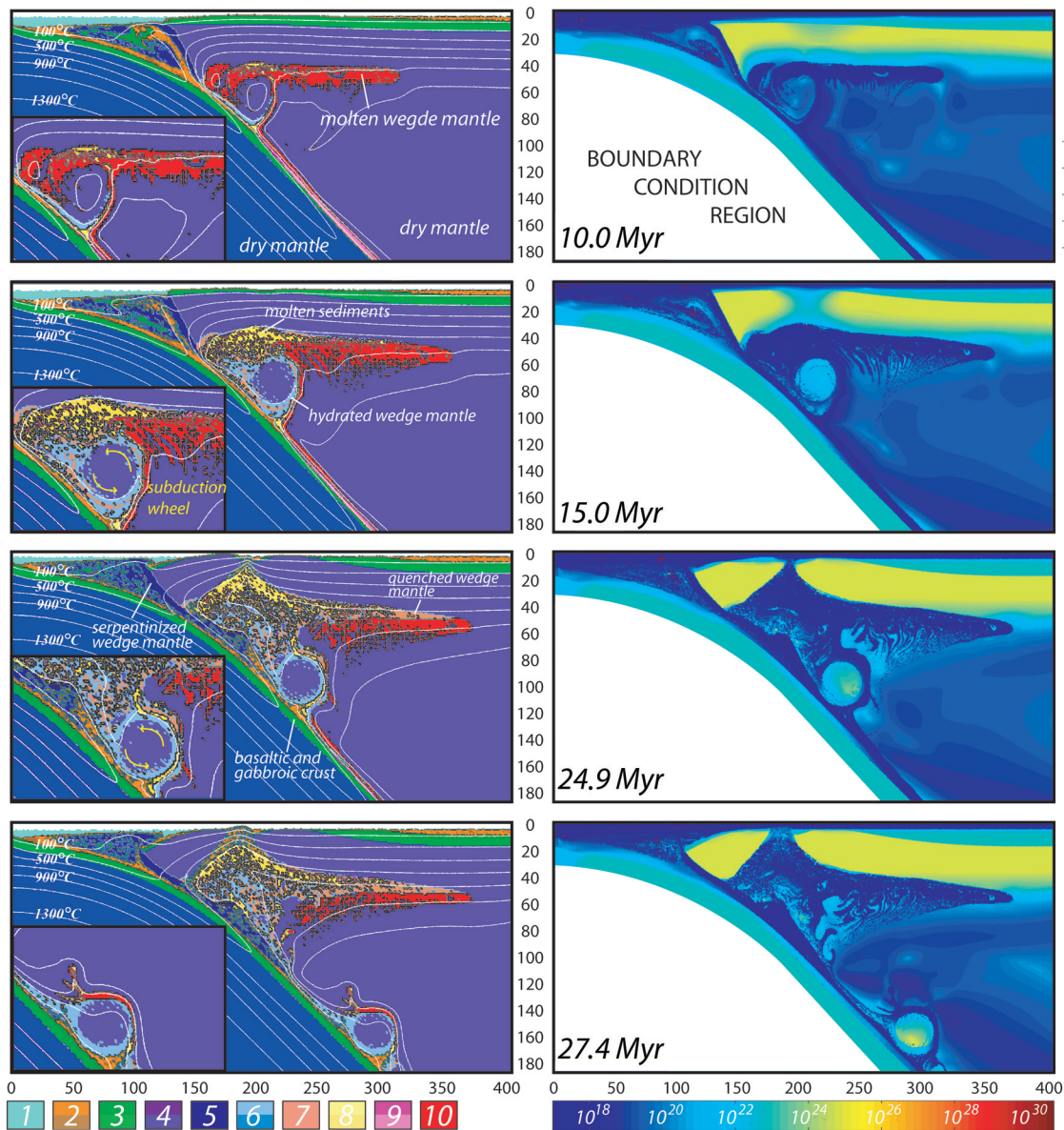


Figure 1. Development of subduction wheel phenomenon (Model 5, Table 1). (left) Evolution of the distribution of different rock types. (right) Distribution of viscosity field (Pa·s). Color code: 1, seawater; 2, sediments; 3, basaltic and gabbroic crust; 4, dry mantle; 5, serpentinized wedge mantle; 6, hydrated wedge mantle; 7, hydrated (quenched) wedge mantle; 8, molten sediments; 9, molten basaltic and gabbroic crust; 10, molten wedge mantle. The main feature of the figure is the rigid wheel: 40 km in diameter, viscosity: 10^{19} to 10^{22} Pa · s as the body descends with subducting slab; it is composed of dry mantle wedge. The body is enveloped by ~6 km thick cold plume material composed of hydrated wedge mantle and molten sediments. Viscosity of plume material is $\sim 10^{17}$. The wheel forms within ~25 Myr. The timescale in all figures corresponds to relative time for the subduction.

downward. If the plume root is not stable and the initiation depth is relatively shallow, the isolation of a fragment of mantle wedge still occurs, but rotation of isolated body quickly becomes unstable and it has no time to cool down and become more rigid and coherent before it vanishes.

[8] The stability of plume initiation is controlled by slab age and rate of subduction (Figure 5). Slow

(<2 cm/yr) as well as high (>5 cm/yr) subduction rate prevent isolated body from achieving stable rotational motion.

3.2. Fore-Arc Spin

[9] Due to decoupling of the subducting and overriding plates [e.g., *Hawkins et al.*, 1984], the arc system may be dominated by extension rather than

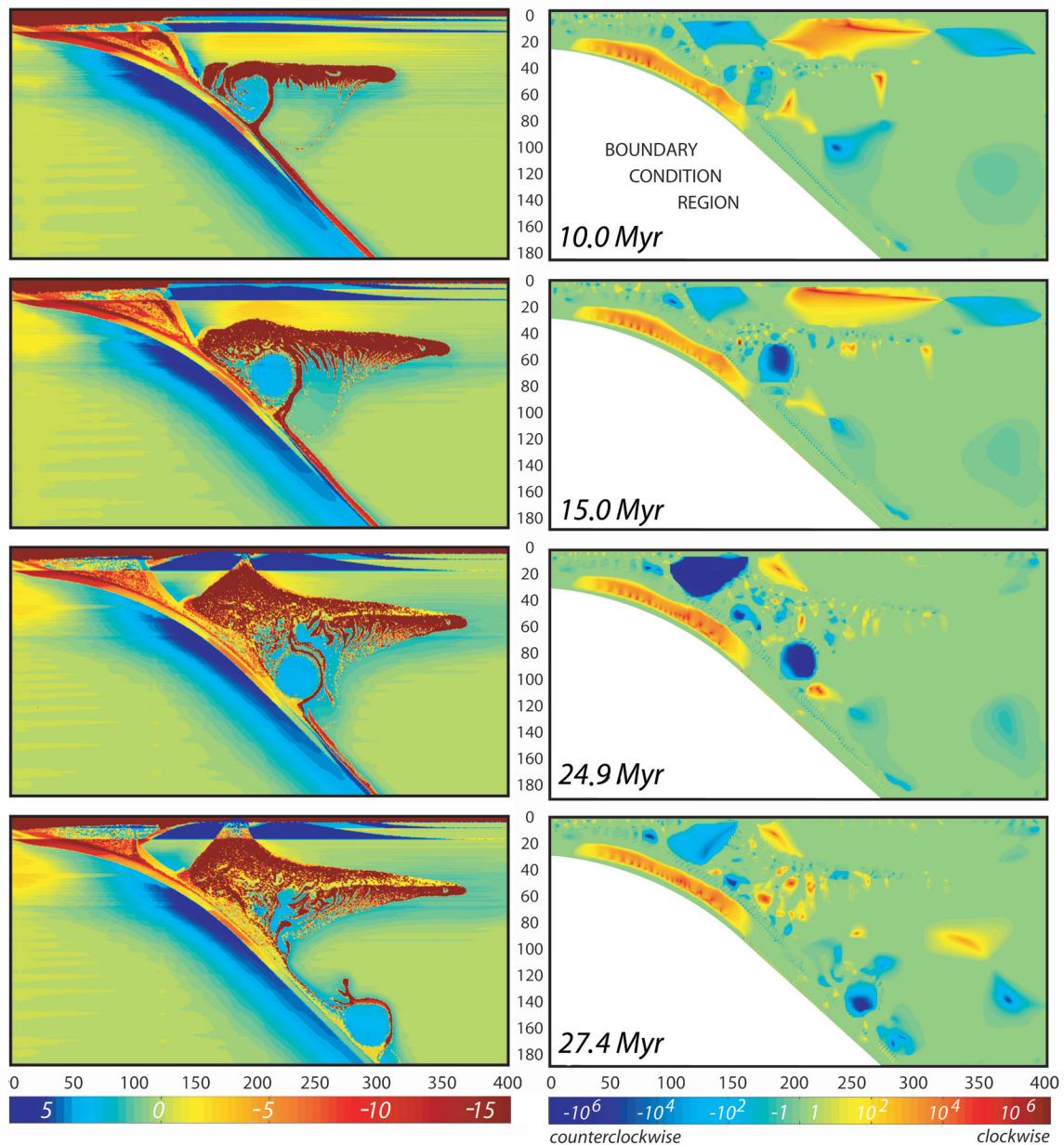


Figure 2. Development of subduction wheel phenomenon (as in Figure 3, Model 5, Table 1). (left) Variations in seismic velocity ($\Delta V_p\%$) are computed relative to vertical profile in the mantle wedge at $x = 350$ km. (right) Relative intensity of rotation $I = \frac{(\frac{\partial v_z}{\partial v_x} - \frac{\partial v_x}{\partial v_z})}{2\dot{\epsilon}_{II}}$, where $\dot{\epsilon}_{II}$ is the second invariant of strain rate tensor. The main feature of the figure is rigid wheel: the seismic velocity anomaly increases by 2% due to dry, cold wedge mantle. The rotation of the body is counterclockwise.

compression. In our experiments, the extension occurs due to the tectonic erosion of weak serpentinized mantle above the slab. Intraarc extension (Figure 6) allows dragging of the fore-arc lithosphere down to a depth of 10–20 km with the subducting slab. In our simulation the burial process is accompanied by the rotational motion of the cold lithospheric fragment of irregular shape trapped between rising hydrated mantle and the subducting slab.

This phenomenon occurs for the subduction rate of 3 cm/yr for a relatively old (80 Myr) subducting slab (Figure 5, Table 1). After ~ 30 Myr, the fore-arc lithosphere is gradually hydrated and dragged downward by subduction erosion within the serpentinized subduction channel.

[10] In our experiments we also observe fore-arc compression, which is a result of plate coupling

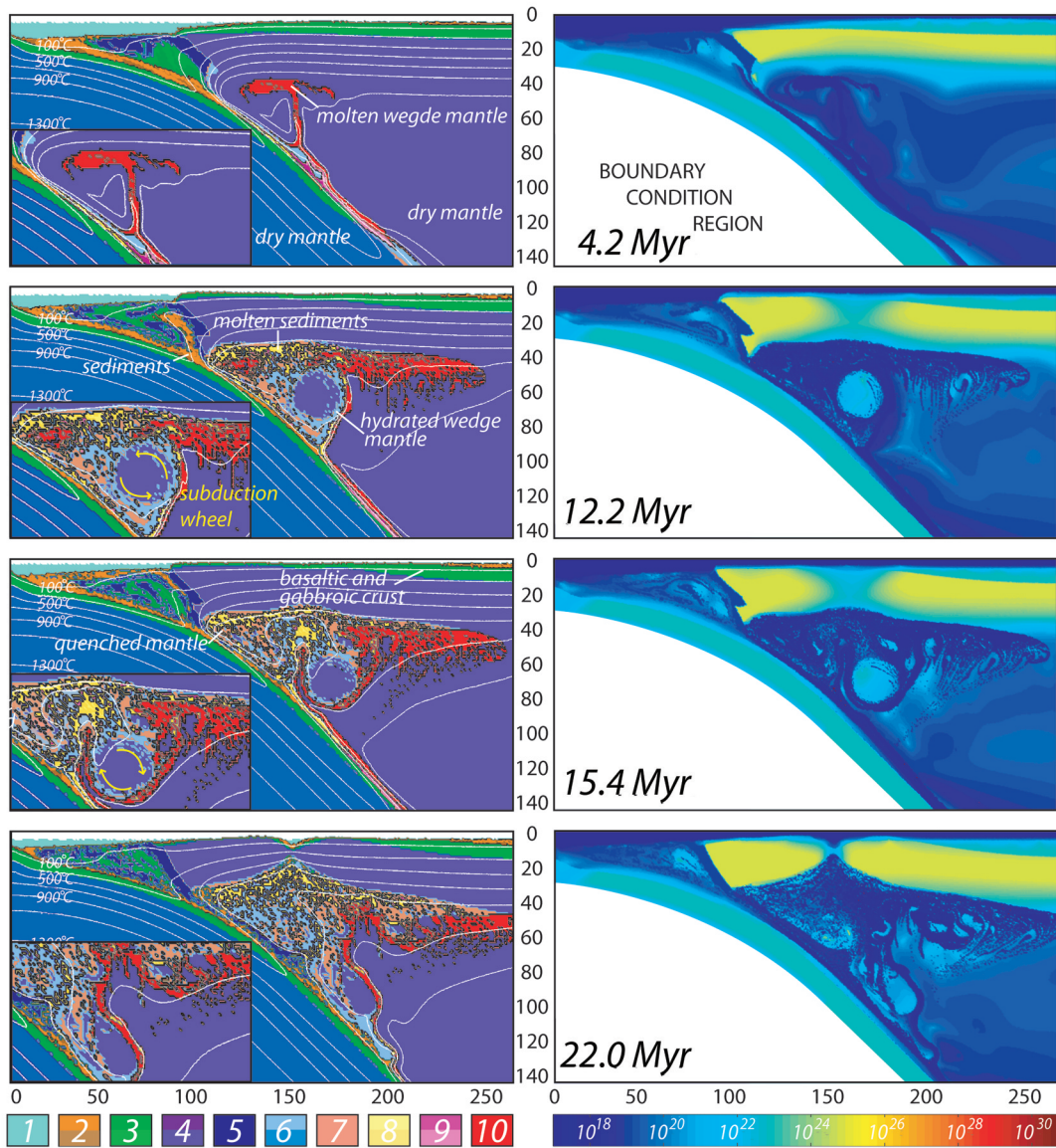


Figure 3. Development of subduction wheel phenomenon (Model 18, Table 1). (left) Evolution of the distribution of different rock types. (right) Distribution of viscosity field (Pa-s). Color code as in Figure 1. The main feature of the figure is the rigid wheel: 45 km in diameter, viscosity: 10^{19} to 10^{20} Pa-s as the body vanishes in the mantle wedge; it is composed of dry wedge mantle. The body is enveloped ~ 5 km thick cold plume material composed of hydrated wedge mantle and molten wedge mantle. Viscosity of plume material is $\sim 10^{17}$.

forces. When the subducting slab is ~ 100 Myr old (Table 1), the compressional forces may lead to deep bending of oceanic crust within the fore-arc region and formation of a deep basin (Figures 7 and 8). The oceanic crust may reach depths of 60 km. As hydrated basaltic crust reaches such a depth it is exposed to high pressure-medium temperature (HP-MP) metamorphism. Over time, there is a transition from a compressional to an extensional regime. This transition forces the fore-arc lithosphere to be dragged to the surface with the

restoring force of subduction channel material. The burial of the fore-arc basin traps the frontal part of the overriding plate wedge between the subduction channel and the buried oceanic crust. The extensional processes coupled with the motion of the rising plume lead to counter-clockwise rotation of this lithospheric fragment.

3.3. Wedge Pinballs

[11] One additional type of spinning structure (wedge “pinballs”) sporadically registered in our

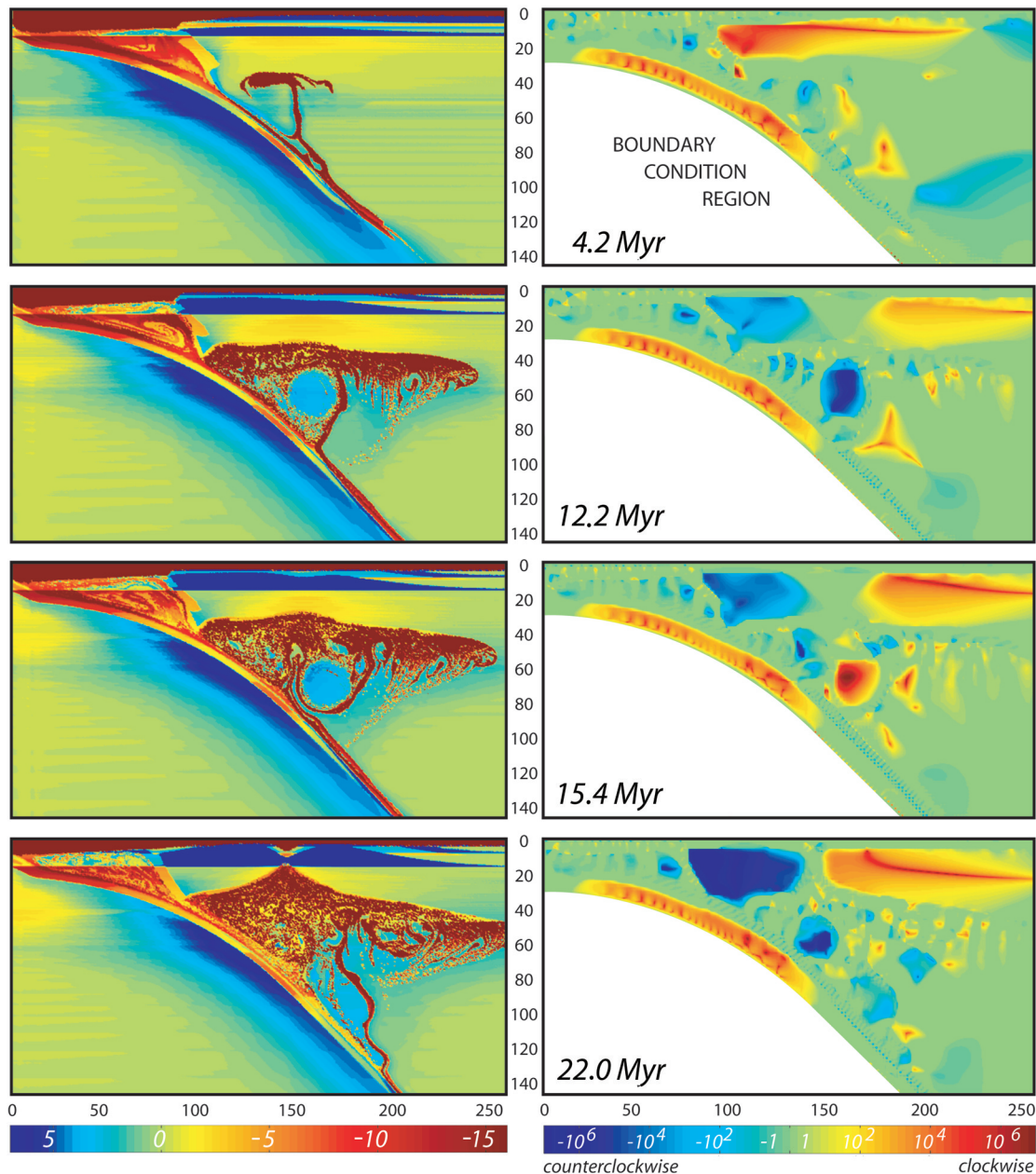


Figure 4. Development of subduction wheel phenomenon (as in Figure 3). (left) Variations in seismic velocity ($\Delta V_p\%$) are computed relative to vertical profile in the mantle wedge at $x = 350$ km. (right) Relative intensity of rotation $I = \frac{(\frac{\partial v_z}{\partial v_x} - \frac{\partial v_x}{\partial v_z})}{2\dot{\epsilon}_{II}}$, where $\dot{\epsilon}_{II}$ is the second invariant of strain rate tensor. The main feature of the figure is the rigid wheel: the seismic velocity anomaly increases by 2% due to dry wedge mantle. The rotation of the body is counterclockwise.

numerical experiments is a small fragment (10–15 km in diameter) of oceanic crust ripped from the overriding plate and caused to rotate within the serpentine channel at a depth of 20–60 km (Figure 7). These rotating bodies are more viscous (10^{19} – 10^{21} Pa·s) than the subduction channel material (10^{18} – 10^{19} Pa·s), but have the same tem-

perature. The temperature of subduction channel is from 100 to 600°C depending on the depth.

4. Discussion and Conclusions

[12] The results presented in this paper are the products of a series of two-dimensional simula-

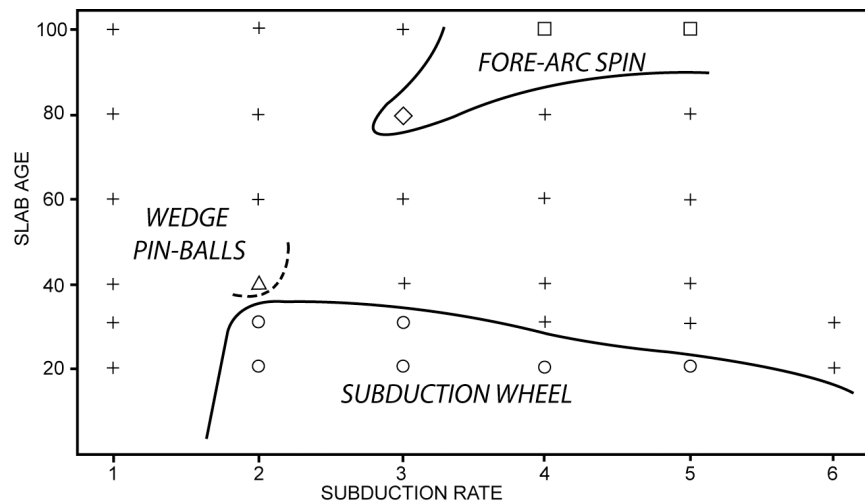


Figure 5. Simplified area diagram for conducted 2-D numerical runs. Cross, runs without rigid body rotation phenomenon; circle, subduction wheel; diamond, fore-arc spin; square, fore-arc spin accompanied by deep basin exhumation; triangle, wedge pinball. Relationship between different physical parameters and rigid body rotation described in Table 1. All remaining runs are listed in Table 2.

tions, which were made calculated with modified I2VIS code of *Gerya and Yuen* [2003b]. Most of the simulations were done with a grid step of 2 km using 101×201 and 0.5 million markers. With this approach we investigated the changes in processes above the subducting slab due to different subduction rate, initial age of subducting slab, viscosity of serpentine and sedimentation/erosion rate, and their dependence on these parameters.

[13] An important aspect is to relate results of our study to subduction processes in three-dimensions. The rigid body phenomenon corresponds to propagation of upwellings released from the slab. Hydration and partial melting along the slab enable development of Rayleigh-Taylor instabilities [*Gerya and Yuen, 2003a*]. This is the leading force for the development of both cold plumes and diapirs. According to 3-D numerical studies of diapirism by *Kaus and Podladchikov* [2001], sheet-like diapiric walls are stable in three dimensions and can propagate rapidly from initial elongated perturbations. We assume therefore that similar wall-like patterns of cold plumes parallel to the trench can develop isolating elliptic and cylindrical spinning rigid bodies in the mantle wedge (Figure 9).

[14] From the predicted seismic velocity anomalies, we can anticipate the tomographic images associated with rigid body rotation. An area of high Q_p (P wave attenuation) surrounded by low Q_p has been observed in the upper mantle below the Salar de Atacama basin [*Schurr et al., 2003*]

(Figure 10). *Schurr et al.* [2003] suggest that this observation can be explained by the presence of a relatively cold and rigid block surrounded by lighter material. Water in the mantle wedge causes partial melting in regions where temperature exceeds the wet solidus of peridotite, and in the sub-solidus region water raises the homologous temperature of the mantle. Both effects lower seismic Q_p ; therefore low Q_p areas are interpreted as fluid or melt pathways in the mantle [*Schurr et al., 2003*]. As low Q_p regions correlate well with low V_p and high Q_p regions correlate to high V_p [*Schurr, 2001*], we suggest that anomalies observed below Salar de Atacama basin are consistent with the subduction wheel model predicted by our simulation (Figures 2, 4, and 10). We speculate that the rigid body phenomena documented in our numerical experiments above subducting slab may play a role in the development of observed isolated positive tomographic anomalies surrounded by negative anomalies.

[15] Fore-arc spin may play a role for the intraarc extension process documented in several subduction zones, as in the Mediterranean region [e.g., *Jolivet and Faccenna, 2000; Faccenna et al., 2003*], or northern Chile [e.g., *Buddin et al., 1993*]. The deep fore-arc basin model may explain the occurrence of two different types (high pressure-low temperature (HP-LT) and high pressure-medium temperature (HP-MT) among contemporaneous metamorphic complexes in the same province. HP-LT and HP-MT metamorphic rocks were observed within the Aegean basin

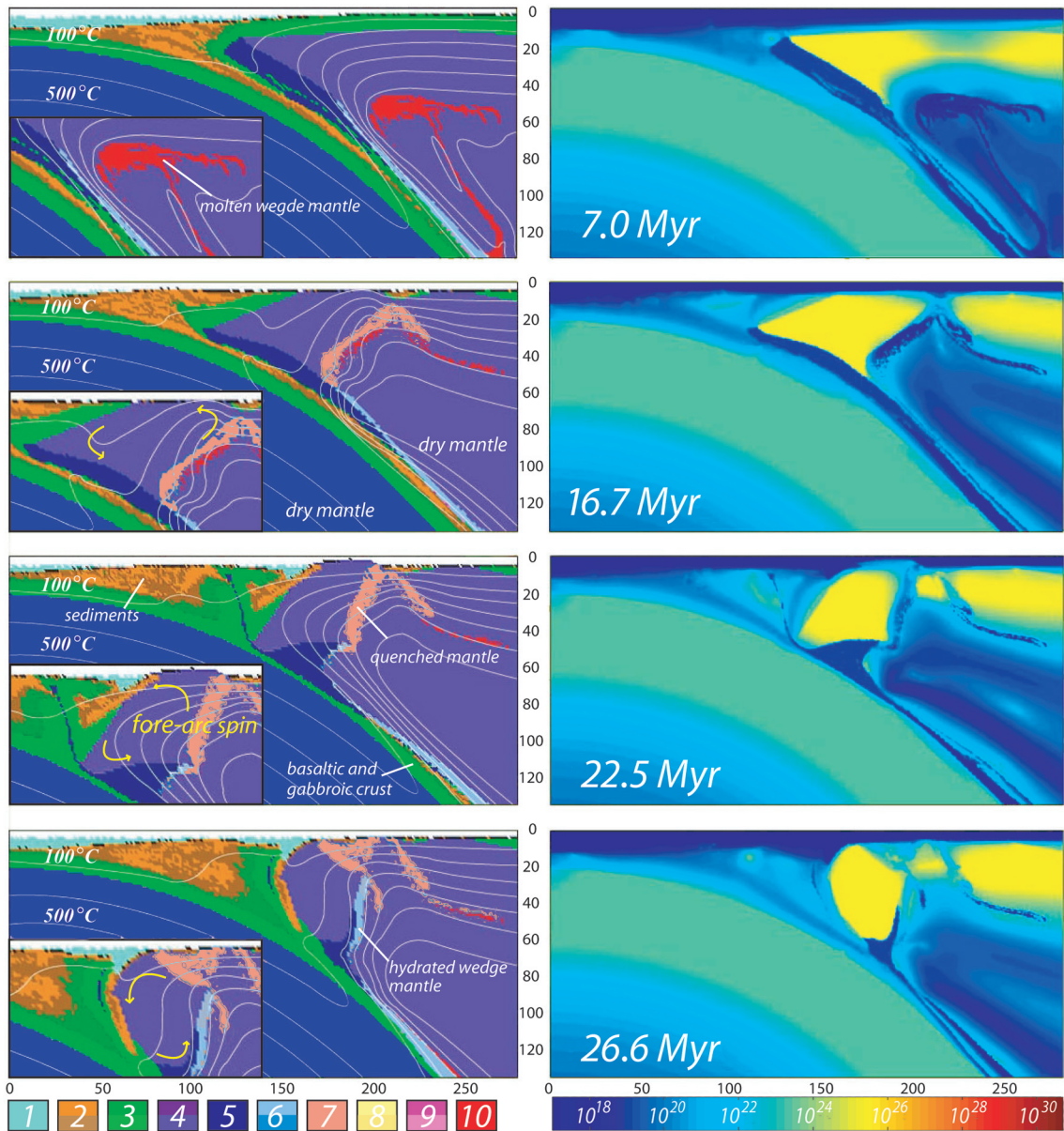


Figure 6. Development of fore-arc spin phenomenon (Model 29, Table 1). (left) Evolution of the distribution of different rock types. (right) Distribution of viscosity field (Pa s). Color code is the same as in Figure 1. The main feature of the figure is the rigid part of the overriding palate isolated by hydrated wedge mantle from dry asthenospheric wedge. Viscosity of the rigid body varies from 10^{20} to 10^{23} .

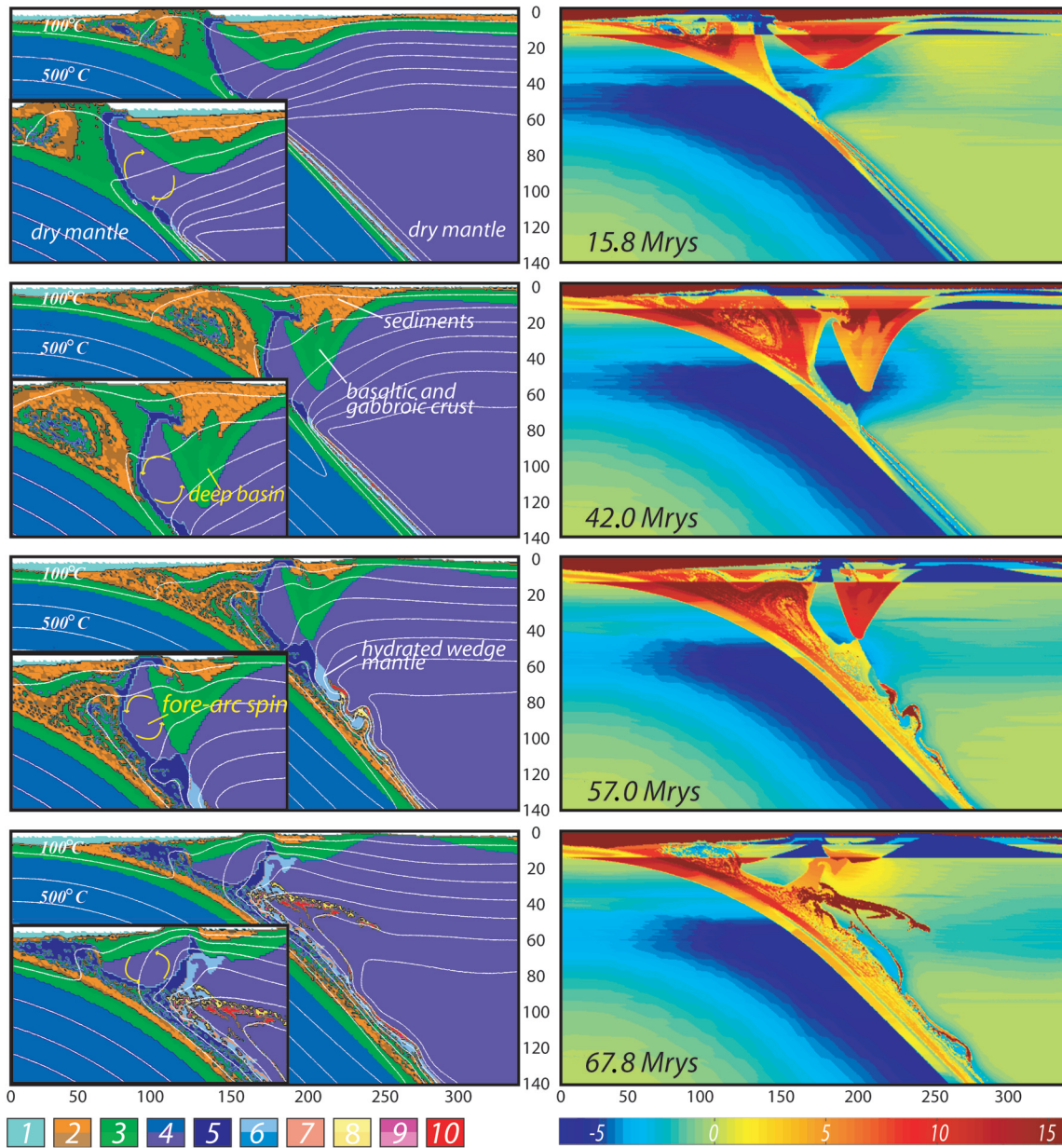
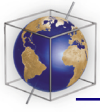


Figure 7. Evolution of burial and exhumation of fore-arc basin (Model 31, Table 1). (left) Evolution of the distribution of different rock types. (Right) Variations in seismic velocity ($\Delta V_p\%$) are computed relative to vertical profile in the mantle wedge at $x = 350$ km. Color code is the same as in Figure 1. The main feature of the figure is buried fore-arc basin that is isolating part of the overriding plate. The rotation of the body is counterclockwise during the exhumation of the body.

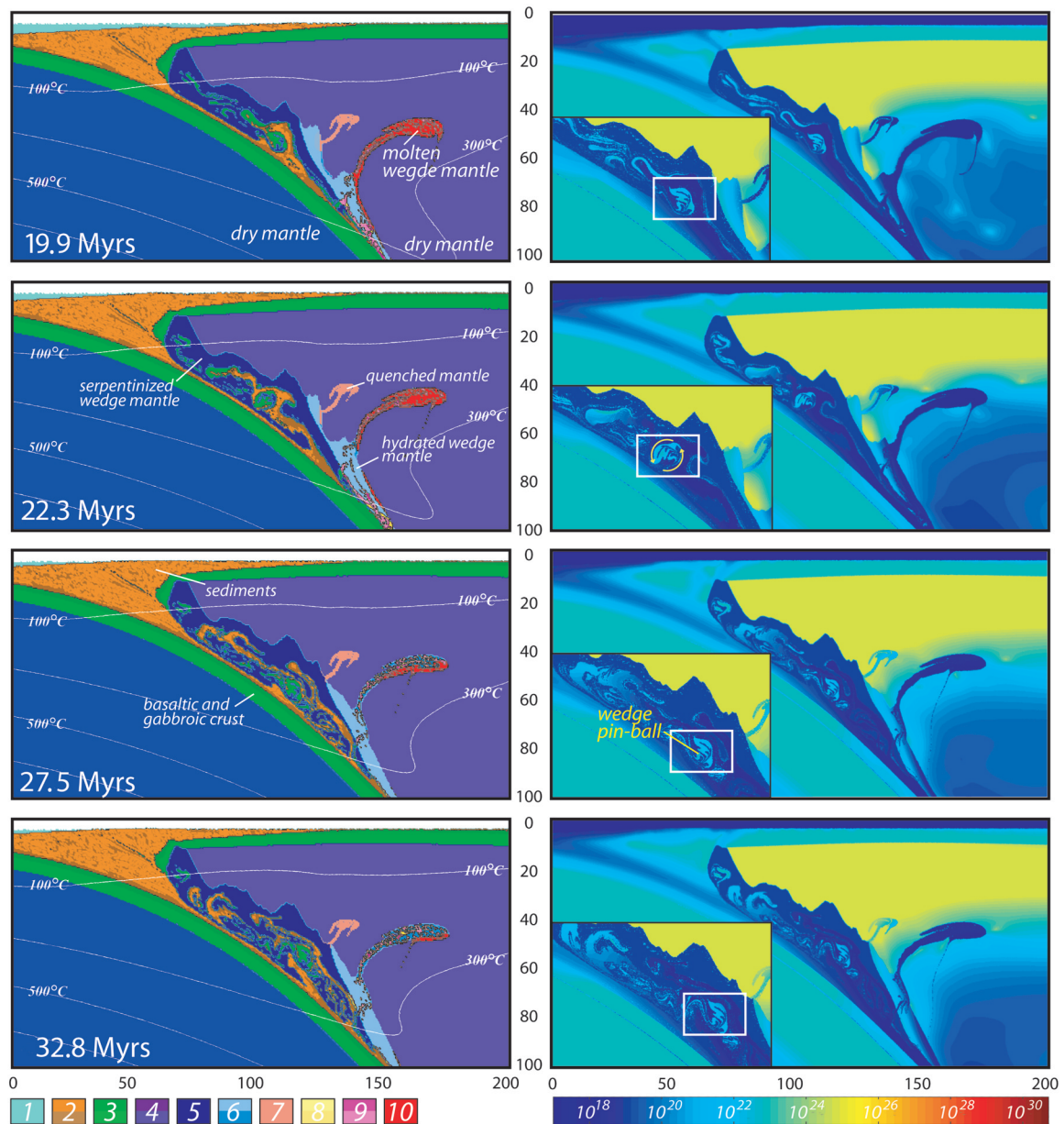


Figure 8. Wedge pinball phenomenon (Model 25, Table 1). (left) Evolution of the distribution of different rock types. (right) Distribution of viscosity field (Pa-s). Color code is the same as in Figure 1. The main feature of the figure is the rigid body of higher viscosity (10^{20} Pa-s) than the channel's material rotating within the subduction channel but having the same temperature.

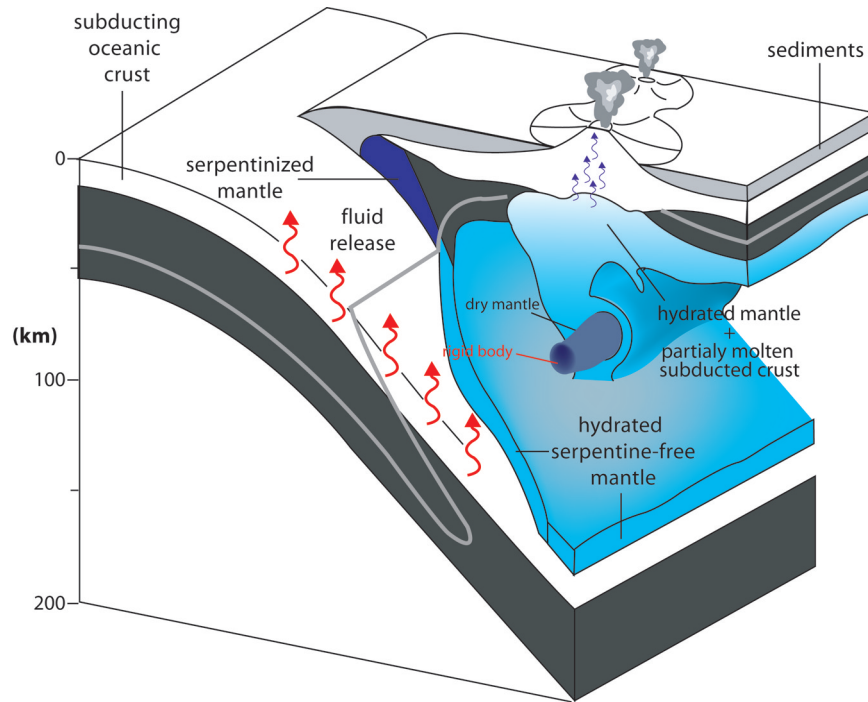


Figure 9. Conceptual development of rigid body rotation in three dimensions.

[Lister *et al.*, 1984]. The HP-LT blueschist formed within this subduction/accretionary complex [Faccenna *et al.*, 2003]. We propose that HP-MT metamorphism occurs in deep fore-arc basins [Lister *et al.*, 1984; Jolivet and Patriat, 1999; Gautier *et al.*, 1999; Faccenna *et al.*, 2003]. Evidence for the transition from compressional to extensional tensional regimes has been observed in the geologic record [Uyeda and Kanamori, 1979]. Our simulation's prediction of deep burial of the fore-arc basin provides an explanation for this geological setting.

[16] Within Champtoceaux metamorphic complex, which is a part of Armorican Massif few metamorphic bodies with accretion mélange were observed [e.g., Ballèvre *et al.*, 2002; Martelet *et al.*, 2004] (Figure 11). These bodies are characterized by coherent chemical and textural structures, which is unusual within material exhumed from subduction channels. The geological setting and size (a dozen or so km in diameter) of these blocks supports the hypothesis that they are pieces of crust ripped from an overriding plate and included as individual components (wedge pinballs, Figures 9 and 11) of a subduction channel.

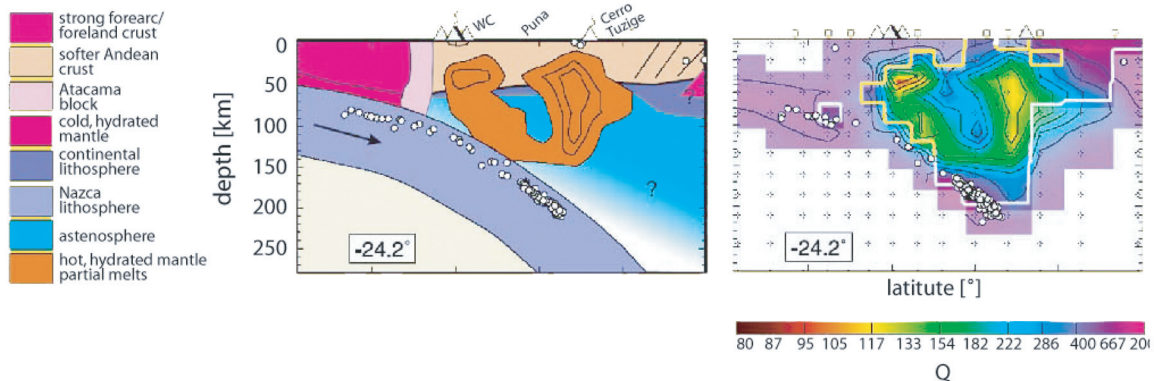


Figure 10. Possible natural example of subduction wheel phenomenon. (left) Interpretations of the cross sections for Q_p at 22.2°S. (right) Cross section for Q at 22.2°S for the central Andean subduction zone. The thick white contour indicates regions of good resolution as measured by the spread value. Regions of poor resolution are drawn in a slightly faded color (modified after Schurr *et al.* [2003]).

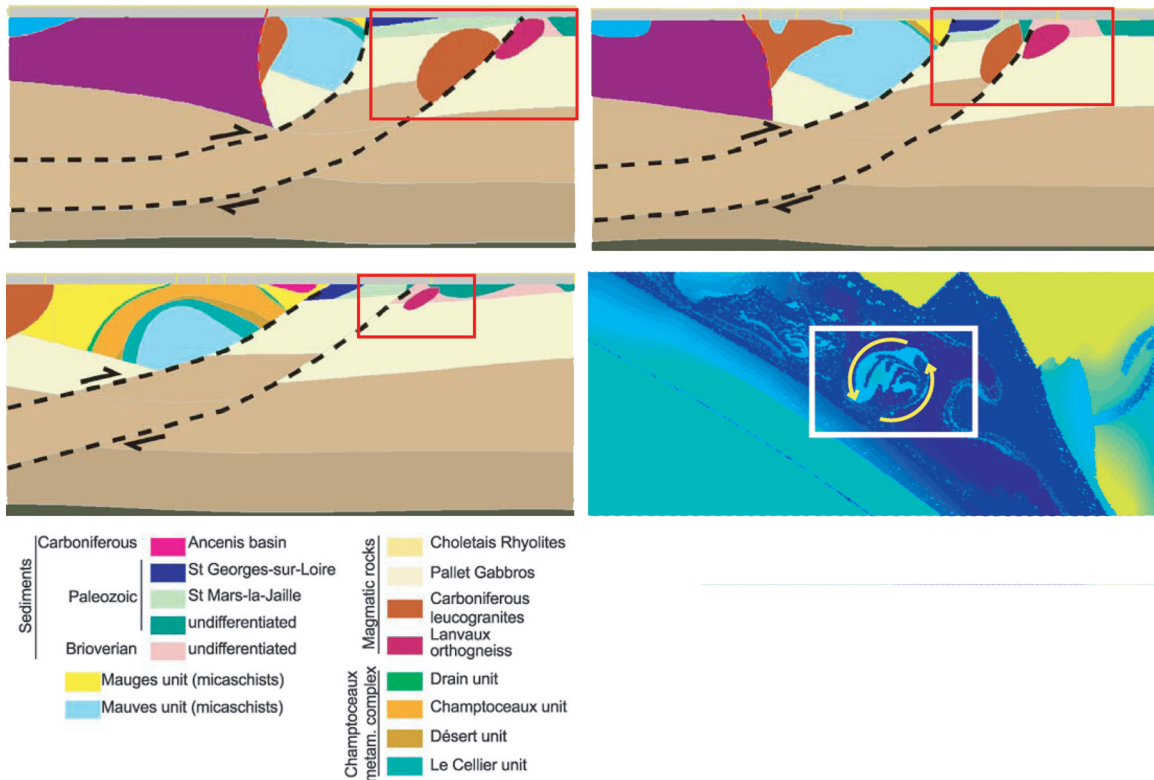


Figure 11. Possible natural example of wedge pinballs. (top left, top right, and bottom left) Cross sections of Champtoceaux area. Within the outlined boxes, metamorphic blocks of coherent chemical and textural structures can be observed (modified after *Martelet et al.* [2004]). (bottom right) A wedge pinball.

[17] On the basis of the results of our numerical study, we conclude that rigid-body motion phenomena are consequences of the hydration and melting above slabs and thus can be considered as features of the subduction process.

Appendix A: Visualization and Computational Challenges

[18] Our highest-resolution simulations to date use 10 billion markers. This extremely high resolution results in uncompressed output file sizes of 210 GB or more for each time step. Similar amounts of memory are required during runs as well, but the latest shared-memory supercomputers such as COBALT at NCSA have ample memory for these large runs. We have implemented a parallel computing with Open MP and a compressed file format for output that is capable of reducing file sizes by at least three orders of magnitude indeed allowing rerunning from the compressed output. Output file compression also allows us to save output to disk more frequently, allowing us to create animations

with higher frame rates than was previously possible. While visualizing the data from this simulation is trivial for low-resolution runs (0.5–2 million markers) where the number of markers is on the same order as the number of pixels on a typical computer screen, the visualization problem becomes much more challenging at higher resolutions, where the number of markers dwarfs the number of pixels on any display device. High-resolution runs are necessary to explore stirring structures at spatial scales on the order of 100 m to 1 m (Figures A1 and A2) [*Rudolph et al.*, 2005]. In order to permit long-distance collaboration without transferring massive amounts of data, we have developed a Web-based visualization solution, WEB-IS4, that is part of our WEB-IS family of Web-based solutions. WEB-IS4 uses an HTML and Javascript front-end coupled with a PHP and C backend to retrieve regions of interest from high-resolution 2-D data sets in real time. Any region of interest can be retrieved from a $n \times 10^{10}$ element data set, converted into an image, and sent over the Web in under 0.25s. The fast response when querying a large data set is achieved by means of

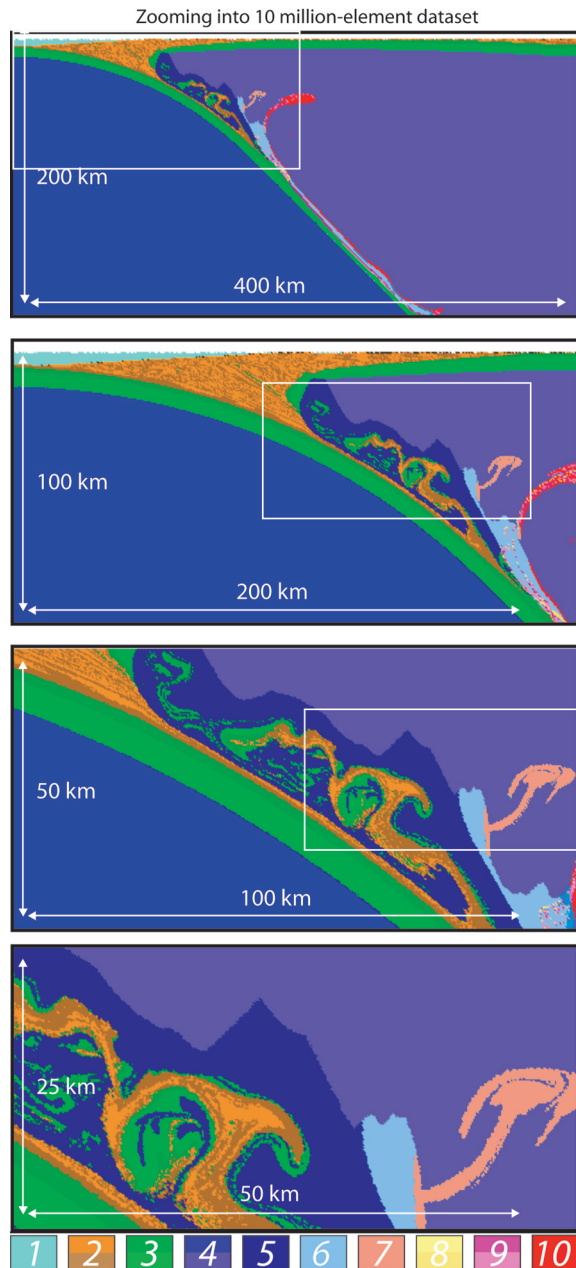


Figure A1. High-resolution multiple scale visualization of mechanical stirring structures related to development of a “wedge pinball.” Compressed output from the numerical experiment with 10 million markers. Color code: 1, seawater; 2, sediments; 3, basaltic and gabbroic crust; 4, dry mantle; 5, serpentinized wedge mantle; 6, hydrated wedge mantle; 7, hydrated (quenched) wedge mantle; 8, molten sediments; 9, molten basaltic and gabbroic crust; 10, molten wedge mantle.

a hierarchical data format. In a hierarchically structured file, the topmost member of the hierarchy is a downsampled version of the original data set whose size is approximately the same as the

desired display size. This member of the hierarchy is used only for regions of interest with low magnification. If a higher magnification is desired, a lower member of the hierarchy is accessed. The backend chooses a member of the hierarchy in such a way that the region of interest image is never upsampled. This permits us to view extremely fine-scale features in the composition field while maintaining a sense of the big picture by zooming into the data set in real time. This hierarchical data retrieval scheme will also allow us to explore large 2-D data sets interactively on display walls by parallelizing the image retrieval process.

B1. Model Design and Numerical Technique

[19] In this appendix we give description of numerical model, initial configuration and thermo-mechanical and petrological technique used.

B2. Initial Configuration

[20] For this set of simulations on an island arc subduction we used 2-D numerical model (Figure B1) with kinematically prescribed subducting plate and with either static [Gerya *et al.*, 2002; Gerya and Yuen, 2003b] or dynamic [Gerya *et al.*, 2006] hydration of the mantle wedge as described below. In this model oceanic crust consists of a relatively thin (1000 m) heterogeneous layer of marine sediments, an upper 2 km thick sequence of hydrothermally altered basalts (metabasalts), and a lower 5 km section composed largely of gabbroic rocks (Table B1). The subjacent mantle is considered to be anhydrous peridotite, whereas the overlying mantle is either anhydrous or hydrated (≤ 2 wt% water) peridotite depending on the kinematic model for the propagation of slab fluids discussed below. Although mantle wedge rocks have the capacity to absorb up to 8 wt% water during serpentinization [Connolly, 2005], we adopt 2 wt% water as an upper limit to account for heterogeneous hydration resulting from channelization of slab-derived fluids [Davies, 1999] as consistent with observed mantle wedge seismic velocities [Carlson and Miller, 2003]. The boundary conditions account for incoming and outgoing asthenospheric flow under the overriding plate. The top surface of the oceanic crust is calculated dynamically as a free surface by using an 8-km-thick hydrosphere with low viscosity (10^{18} Pa · s) and density (1 kg/m^3 for the atmosphere, 1000 kg/m^3 for seawater). The interface between this weak layer and the top of the oceanic crust deforms

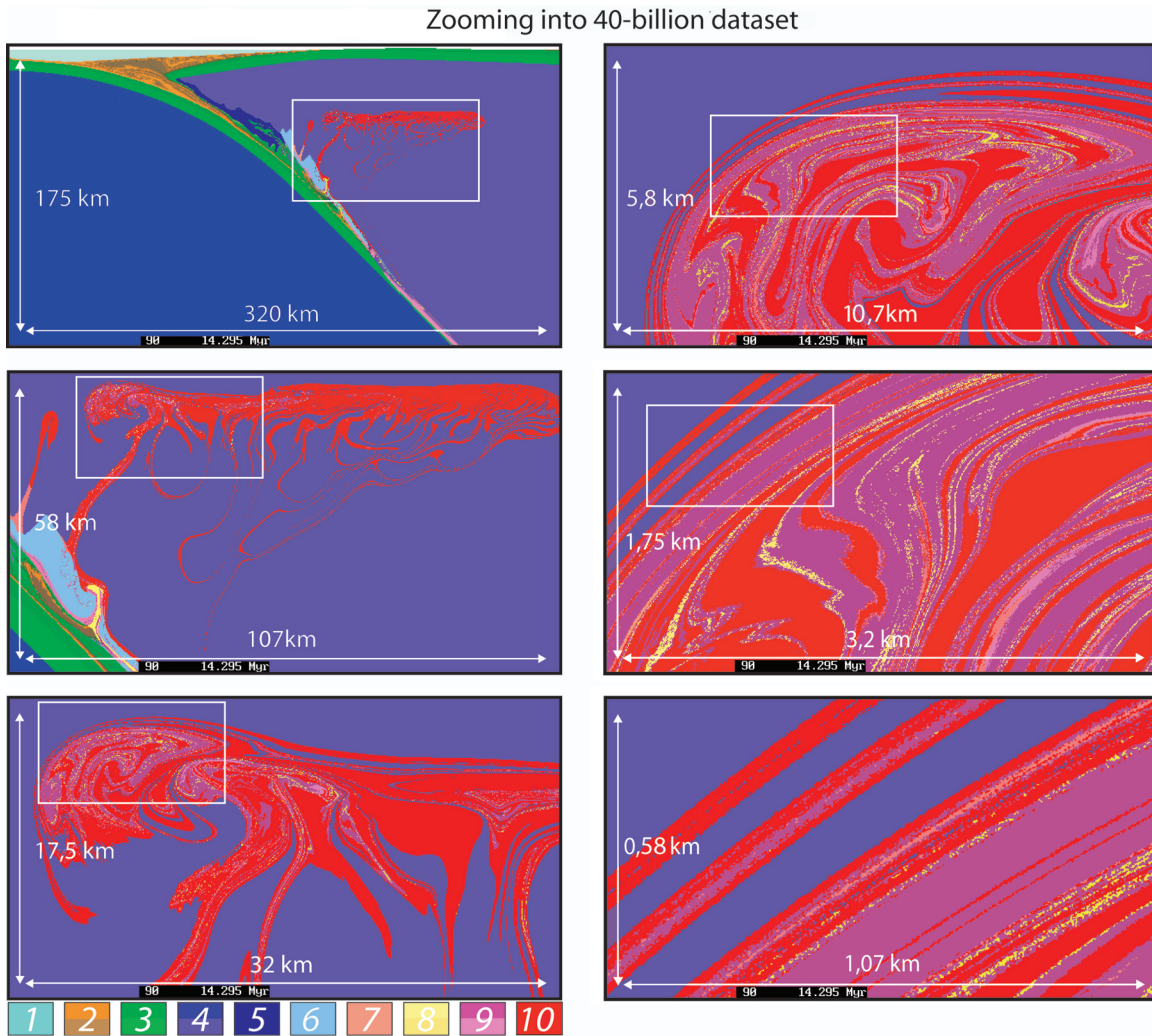


Figure A2. High-resolution multiple scale visualization of mechanical stirring structures related to development of a “cold plume.” Forty billion element (pixel) data set with spatial resolution of ~ 2 m is based on compressed output from the numerical experiment with 10 billion markers. Color code is the same as in Figure A1.

spontaneously and is treated as an erosion/sedimentation surface which evolves according to transport equation (in Eulerian coordinates) solved at each time-step [Gerya and Yuen, 2003b].

$$\partial z_{es}/\partial t = v_z - v_x \partial z_{es}/\partial x - v_s + v_e \quad (\text{B1})$$

where z_{es} is a vertical position of the surface as a function of the horizontal distance x ; v_z and v_x are the vertical and horizontal components of material velocity vector at the surface v_s and v_e are sedimentation and erosion rates, respectively, which correspond to the relation:

$$v_s = 0 \text{ mm/a}, v_e = v_{e0} \quad \text{when } z < 4 \text{ km},$$

$$v_s = v_{s0} \text{ mm/a}, v_e = 0 \quad \text{when } z < 4 \text{ km},$$

where v_{e0} and v_{s0} are imposed erosion and sedimentation rates, respectively. Erosion and sedimentation processes are implemented via marker transmutation. The viscosity of the hydrosphere ($10^{18} \text{ Pa} \cdot \text{s}$) creates a high viscosity contrast ($>10^3$) and causes minimal shear stresses ($<10^4 \text{ Pa}$) along the erosion/sedimentation surface. As follows from our test experiments further lowering of hydrosphere viscosity does not affect dynamics of this surface. Accounting for the thermal and density effects of phase transformations poses a significant challenge [Bittner and Schmeling, 1995; Barboza and Bergantz, 1997; Vasilyev et al., 2004] because abrupt changes associated with the appearance of a phase are difficult to handle numerically, particularly in the continuity condition. To overcome these difficulties, we employ the incompressible fluid approximation for the con-

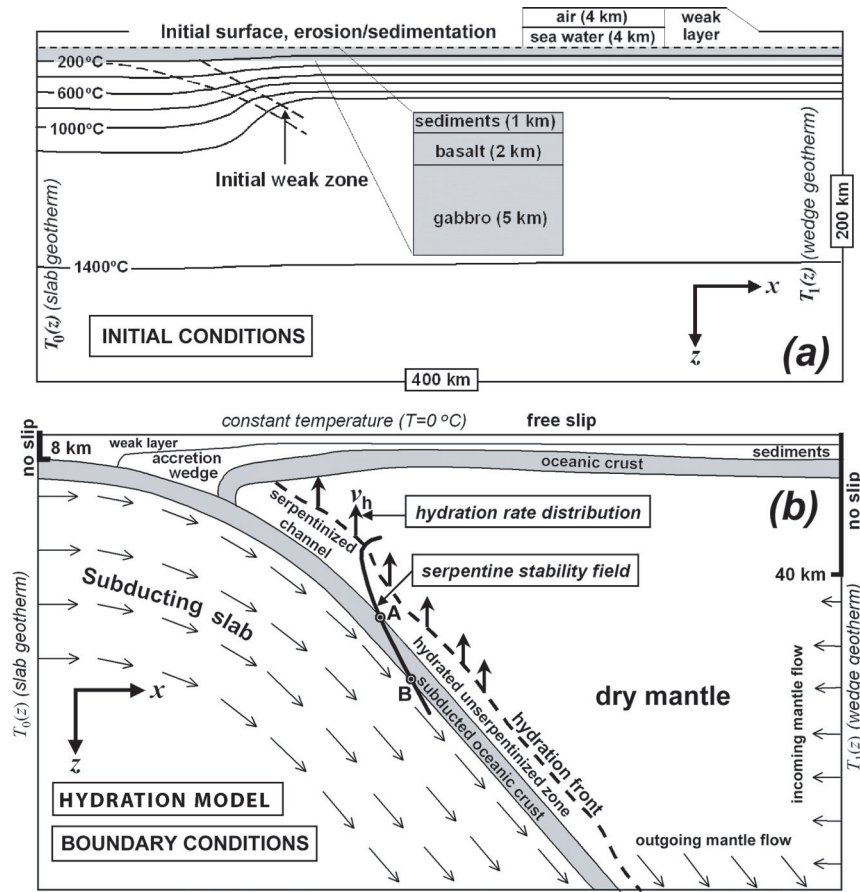


Figure B1. Numerical upper-mantle model designed for our two-dimensional numerical experiments. (a) Initial conditions for calculation are taken as follows: the initial position of the subduction zone is prescribed by a weak, 6-km-thick, hydrated peridotite layer; initial temperature field in subducting plate is defined by an oceanic geotherm $T_0(z)$ with a specified age; initial temperature distribution in overriding plate $T_1(z)$ corresponds to equilibrium thermal profile with 0°C at surface and 1350°C at 32 km depth; initial structure of 8-km-thick oceanic crust is taken as follows (from top to bottom): sedimentary rocks = 1 km, basaltic layer = 2 km, gabbroic layer = 5 km. (b) Boundary conditions and hydration model are shown for the intermediate stage of calculation with well-developed hydrated mantle zone. A and B are intersection points of serpentine stability field with the upper and lower surfaces, respectively, of the oceanic crust. Further details of model design and limitations are given by *Gerya and Yuen* [2003a].

tinuity equation and numerical smoothing of thermal and density effects due to phase changes for the momentum and temperature equation [Gerya *et al.*, 2004c]. Transport and physical properties are then computed by finite differences and a marker-in-cell technique [Gerya *et al.*, 2000; Gerya and Yuen, 2003b].

B3. Numerical Approach

[21] The momentum, continuity, and thermal equations for the two-dimensional creeping-flow, accounting for both thermal and chemical buoyancy, are solved using the I2VIS code [Gerya and Yuen, 2003b] based on conservative finite differences and a nondiffusive-marker-in-cell technique. The ther-

mal equation is formulated as [Gerya and Yuen, 2003b]

$$\rho c_p \left(\frac{DT}{Dt} \right) = -\frac{\partial q_x}{\partial x} - \frac{\partial q_z}{\partial z} + H_r + H_a + H_s + H_L \quad (\text{B2})$$

$$q_x = -k(T, C) \frac{\partial T}{\partial x} \quad q_z = -k(T, C) \frac{\partial T}{\partial z},$$

$$H_a = T \alpha \frac{DP}{Dt} \quad H_s = \sigma_{xx} \dot{\epsilon}_{xx} + \sigma_{zz} \dot{\epsilon}_{zz} + 2\sigma_{xz} \dot{\epsilon}_{xz},$$

where D/Dt is the substantive time derivative; x and z denote, respectively, the horizontal and vertical coordinates; σ_{xx} , σ_{xz} , σ_{zz} are components of the deviatoric stress tensor; $\dot{\epsilon}_{xx}$, $\dot{\epsilon}_{xz}$, $\dot{\epsilon}_{zz}$ are

Table B1. Model Rock Compositions^a

	Sediment	Upper Oceanic Crust (Altered Basalt)	Lower Oceanic Crust (Gabbro)	Mantle (Peridotite)
SiO ₂	61.10	47.62	53.49	45.55
Al ₂ O ₃	12.43	14.48	14.07	4.03
FeO	5.43	10.41	6.86	7.47
MgO	2.59	6.92	12.07	37.42
CaO	6.21	13.39	10.73	3.18
Na ₂ O	2.54	2.15	1.22	0.33
K ₂ O	2.13	0.58	0.09	0.03
H ₂ O ^b	7.60	2.78	1.47	1.98

^aRock compositions are in weight%. Sediment is the GLOSS average [Plank and Langmuir, 1998]; basalt is an average for the upper 500 m of the igneous section of the oceanic crust [Staudigel et al., 1989]; gabbro is a synthetic composition for the gabbroic section of the oceanic crust [Behn and Kelemen, 2003], modified to contain up to 1.5 wt% water to represent the effects of lower crustal hydrothermal alteration [Carlson, 2003], and peridotite is the LOSIMAG composition [Hart and Zindler, 1986] chosen to represent mantle peridotite. The compositions have been simplified by the omission of minor elements such as Mn, P, Ti, and Cr and the assumption that all Fe is ferrous; additionally, CO₂ has been removed from the GLOSS sediment composition.

^bMaximal H₂O content in the rocks (see text for details of water balance at elevated P and T).

components of the strain rate tensor in; P is pressure; T is temperature; q_x and q_z are heat fluxes; ρ is density; g is gravitational acceleration; $k(T, C)$ is the thermal conductivity, a function of composition and temperature (Table B2 [e.g., Thompson and Connolly, 1995]; C_p is the isobaric

heat capacity; H_r , H_a , H_s , and H_L denote, respectively, radioactive, adiabatic, shear and latent heat production.

[22] The effective creep viscosities of solid rocks are represented as a function of temperature and stress by experimentally determined flow laws (Table B3). Partially molten rocks are assigned a reduced effective viscosity [e.g., Pinkerton and Stevenson, 1992] of 10^{17} Pa · s.

B4. Obtaining Mineralogy

[23] The stable mineralogy for each lithology are obtained by free energy minimization [Connolly and Pettrini, 2002] as a function of pressure and temperature from thermodynamic data (Table B2). For this purpose, phase relations were resolved on a grid with a resolution of 5 K and 25 MPa. The range of physicochemical conditions considered here requires extrapolation of the silicate melt model [Ghiorso et al., 2002]. Therefore, to ensure consistency with experimentally constrained melting boundaries employed in our earlier work [Gerya and Yuen, 2003a], calculations were done for each lithology both with and without the silicate melt model. Physical properties were then computed from the appropriate results depending upon whether melt was predicted to be stable from the experimentally constrained phase relations (Table B3). Examples of phase diagrams computed for different lithologies are discussed by [Connolly

Table B2. Phases and Thermodynamic Data Sources^a

Phase	Formula	Source
Antigorite	Mg _{48x} Fe _{48(1-x)} Si ₃₄ O ₈₅ (OH) ₆₂	Rupke et al. [2004]
Clinoamphibole	Ca _{2-2w} Na _{z+2w} Mg _{(3+2y+z)x} Fe _{(3+2y+z)(1x)} Al _{3-y-w} Si _{7+w+y} O ₂₂ (OH) ₂ , $w + y + z \leq 1$	Wei and Powell [2003]; White et al. [2003]
Biotite	KMg _{(3-w)x} Fe _(3-w) (1-x)Al _{1+2w} Si _{3-w} O ₁₀ (OH) ₂ , $x + y \leq 1$	Powell and Holland [1999]
Chlorite	Mg _{(5-y+z)x} Fe _(5-y+z) (1-x)Al _{2(1+y-z)} Si _{3-y+z} O ₁₀ (OH) ₈	Holland et al. [1998]
Coesite	SiO ₂	
Clinopyroxene	Na _{1y} Ca _y Mg _{xy} Fe _{(1-x)y} Al _y Si ₂ O ₆	Holland and Powell [1996]
Fluid	H ₂ O	Connolly and Trommsdorff [1991]
Garnet	Fe _{3x} Ca _{3y} Mg _{3(1-x-y)} Al ₂ Si ₃ O ₁₂ , $x + y \leq 1$	Holland and Powell [1998]
Kyanite	Al ₂ SiO ₅	
Lawsonite	CaAl ₂ Si ₂ O ₇ (OH) ₂ ·(H ₂ O)	
Mica	K _x Na _{1-x} Mg _y Fe _z Al _{3-2(y+z)} Si _{3+y+z} O ₁₀ (OH) ₂	Holland and Powell [1998]
Melt	Na-Mg-Al-Si-K-Ca-Fe hydrous silicate melt	Ghiorso et al. [2002]
Olivine	Mg _{2x} Fe _{2(1-x)} SiO ₄	Holland and Powell [1998]
Orthopyroxene	Mg _{x(2-y)} Fe _{(1-x)(2-y)} Al _{2y} Si _{2-y} O ₆	Holland and Powell [1996]
Plagioclase	Na _x Ca _{1-x} Al _{2x} Si _{2+x} O ₈	Newton et al. [1980]
Sanidine	Na _x K _{1-x} AlSi ₃ O ₈	Thompson and Hovis [1979]
Stishovite	SiO ₂	
Talc	Mg _{(3-y)x} Fe _(3-y) (1-x)Al _{2y} Si _{4y} O ₁₀ (OH) ₂	Holland and Powell [1998]

^aUnless indicated otherwise, thermodynamic data were taken from Holland and Powell [1998] (revised 2002). The compositional variables w , x , y , and z may vary between zero and unity and are determined as a function of pressure and temperature by free-energy minimization. Thermodynamic data for the iron end-member for antigorite solution were estimated as described by Rupke et al. [2004].

Table B3. Material Properties Used in 2-D Numerical Experiments

Material	Thermal Conductivity, W/(m K)	Rheology	P-T Conditions of Wet Solidus
Sedimentary rocks	$0.64 + \frac{807}{T+77}$	wet quartzite flow law	$889 + \frac{17900}{P+54} + \frac{20200}{(P-54)^2}$ at $P < 1200$ MPa, $831 + 0.06P$ at $P > 1200$ MPa
Upper oceanic crust (altered basalt)	$1.18 + \frac{474}{T+77}$	wet quartzite flow law	$97 - \frac{7040}{P+354} + \frac{7780}{(P+354)^2}$ at $P < 1600$ MPa, $935 + 0.0035P + 0.0000062P^2$ at $P > 1600$ MPa
Lower oceanic crust (gabbro)	-/-	plagioclase (An75) flow law	-/-
serpentinized mantle	$0.73 + \frac{1293}{T+77}$	constant viscosity $10^{18} - 10^{19}$ Pa s	-
Hydrated unserpentinized mantle ^a	-/-	wet olivine flow law	$1240 + \frac{49800}{P+323}$ at $P < 2400$ MPa, $1266 - 0.0118P + 0.0000035P^2$ at $P > 2400$ MPa
Dry mantle	-/-	dry olivine flow law	-
References	<i>Clauser and Huenges</i> [1995]	<i>Gerya et al.</i> [2002]; <i>Ranalli</i> [1995]	<i>Schmidt and Poli</i> [1998]; <i>Poli and Schmidt</i> [2002]

^aHydrated mantle beyond the serpentine stability field [*Schmidt and Poli*, 1998], $T > 751 + 0.18 P - 0.000031 P^2$ at $P < 2100$ MPa, $T > 1013 - 0.0018 P - 0.0000039 P^2$ at $P > 2100$ Mpa.

and *Kerrick*, 2002; *Kerrick and Connolly*, 2001a, 2001b].

B5. Seismic Velocity Calculation

[24] Seismic velocities were calculated as outlined by *Connolly and Kerrick* [2002], with shear moduli as summarized by *Connolly* [2005]. In the absence of textural information, aggregate seismic velocities are typically computed as an equally weighted combination of the geometric and arithmetic means of the velocities of the constituent minerals, i.e., Voigt-Reuss-Hill averaging [*Bina and Helffrich*, 1992]. Because the geometric mean vanishes if a constituent velocity approaches zero, as is the case for the shear wave velocity in melt, the Voigt-Reuss-Hill scheme leads to profound shear wave velocity anomalies even if the amount of melt is negligible. As we are concerned with the prediction of such anomalies, we have computed aggregate velocities from volumetrically weighted arithmetic mean velocity. This approach assures a conservative model in that it minimizes the effect we are attempting to simulate. The aggregate velocities include the effects of silicate melt but do not account for the presence of free water, the amount of which is assumed to be negligible. Examples of computed seismic velocities are discussed by *Connolly and Kerrick* [2002] and *Connolly* [2005].

B6. Hydration of the Mantle Wedge

[25] At the onset of subduction the lithologies in the oceanic crust are assigned the water contents indicated in Table 1 and the surrounding mantle is

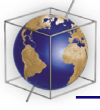
anhydrous. To simulate the migration of water released by dehydration reactions, if water is found to be a stable phase at a particular depth the water is propagated instantaneously upward, until it reaches a rock which contains amount of water which is less than: upper limit of water content adopted for this specific rock type (Table 1) and maximal amount of water that can be consumed by all water-bearing minerals of equilibrium mineral assemblage stable in the rock. Although the limits of water content are to some degree arbitrary, this approach provides a rough estimate for the position of the hydration front that develops in the mantle wedge as a result of slab devolatilization. To formulate this method analytically we compute the vertical velocity of the hydration front from the transport equation [*Gerya et al.*, 2002]

$$\partial z_{h(x)}/\partial t = v_z - v_x \partial z_{h(x)}/\partial x - v_{h(x)}, \quad (\text{B3})$$

where $z_{h(x)}$ is the depth of the hydration front at the horizontal coordinate x ; $v_{h(x)}$ is the substantive hydration rate along the hydration front; and v_z and v_x are the vertical and horizontal components of the material velocity vector at the hydration front. To obtain $v_{h(x)}$, the mass balance equation for water as

$$\int_{z=z_{h(x)}}^{z_{\max}} \frac{D(X_{\text{H}_2\text{O}(x,z)})}{Dt} \rho_{(x,z)} dz = -v_{h(x)} X_{\text{H}_2\text{O}(x,z_{h(x)})} \rho_{(x,z_{h(x)})}, \quad (\text{B4})$$

where: z is depth (z_{\max} corresponds to the lower boundary of the model); $X_{\text{H}_2\text{O}(x,z)}$ and $\rho_{(x,z)}$ are the local water content (weight fraction) and density (kg/m^3) of the rocks beneath the hydration front;



$X_{\text{H}_2\text{O}(x,z,h(x))}$ and $\rho_{(x,z,h(x))}$ are, respectively water contents and density of hydrated mantle on the hydration front; D/Dt represents the substantive time derivative computed for moving rocks by using a marker method. Equations (B3) and (B4) are solved after each time step of the thermo-mechanical model, using the densities and water contents determined by free energy minimization for the relevant lithologies and pressure-temperature conditions. In addition to water-bearing minerals at low temperature ($T < 573$ K) and pressure ($P < 1$ GPa), free water is present in sediments and basaltic crust. Pore water content ($X_{\text{H}_2\text{O}(p)}$) is assumed to decrease linearly with both P and T as

$$X_{\text{H}_2\text{O}(p)} = X_{\text{H}_2\text{O}(p0)} \left(\frac{573 - T(K)}{300} \right) \times (1 - P(\text{GPa})), \quad (\text{B5})$$

where $X_{\text{H}_2\text{O}(p0)}$ is the water content at $T = 273$ K and $P = 0.1$ MPa. Here we take $X_{\text{H}_2\text{O}(p0)} = 2$ wt% as a conservative estimate of the water content for both sediments and basaltic crust.

Acknowledgments

[26] This work was supported by ETH Research Grant TH-12/04-1, by RFBR grant 06-05-64098, by the RF President Program “Leading Scientific School of Russia” (grant HIII-5338.2006.5) to T.V.G., and by CSEDI and ITR programs of the National Science Foundation. We would like to thank to Niel Manktellow and Christian Teyssier for discussion.

References

Ballèvre, M., R. Capdevila, C. Guerrot, and J.-J. Peucat (2002), Discovery of an alkaline orthogneiss in the eclogite-bearing Cellier Unit (Champtoceaux Complex, Armorican Massif): A new witness of the Ordovician rifting, *Geoscience*, *334*, 303–311.

Barboza, S. A., and G. W. Bergantz (1997), Melt productivity and rheology: Complementary influences on the progress of melting, *Numer. Heat Transfer, Part A*, *31*(4), 375–392.

Behn, M. D., and P. B. Kelemen (2003), Relationship between seismic P-wave velocity and the composition of anhydrous igneous and meta-igneous rocks, *Geochem. Geophys. Geosyst.*, *4*(5), 1041, doi:10.1029/2002GC000393.

Billen, M. I., and M. Gurnis (2001), A low viscosity wedge in subduction zone, *Earth Planet. Sci. Lett.*, *193*, 227–236.

Bina, C. R., and G. Helffrich (1992), Calculation of elastic properties from thermodynamic equation of state principles, *Annu. Rev. Earth Planet. Sci.*, *20*, 527–552.

Bittner, D., and H. Schmeling (1995), Numerical modeling of melting processes and induced diapirism in the lower crust, *Geophys. J. Int.*, *123*(1), 59–70.

Buddin, T. S., I. G. Stimpson, and G. D. Williams (1993), North Chilean forearc tectonics and Cenozoic plate kinematics, *Tectonophysics*, *22*, 193–203.

Carlson, R. L. (2003), Bound water content of the lower oceanic crust estimated from modal analyses and seismic velo-

cities of oceanic diabase and gabbro, *Geophys. Res. Lett.*, *30*(22), 2142, doi:10.1029/2003GL018213.

Carlson, R. L., and D. J. Miller (2003), Mantle wedge water contents estimated from seismic velocities in partially serpentinized peridotites, *Geophys. Res. Lett.*, *30*(5), 1250, doi:10.1029/2002GL016600.

Clauser, C., and E. Huenges (1995), Thermal conductivity of rocks and minerals, in *Rock Physics and Phase Relations, AGU Ref. Shelf*, vol. 3, edited by T. J. Ahrens, pp. 105–126, AGU, Washington, D. C.

Connolly, J. A. D. (2005), Computation of phase equilibria by linear programming: A tool for geodynamic modeling and its application to subduction zone decarbonation, *Earth Planet. Sci. Lett.*, *236*, 524–541.

Connolly, J. A. D., and D. M. Kerrick (2002), Metamorphic controls on seismic velocity of subducted oceanic crust at 100–250 km depth, *Earth Planet. Sci. Lett.*, *204*(1–2), 61–74.

Connolly, J. A. D., and K. Pettrini (2002), An automated strategy for calculation of phase diagram sections and retrieval of rock properties as a function of physical conditions, *J. Metamorph. Petrol.*, *20*, 697–708.

Connolly, J. A. D., and V. Trommsdorff (1991), Petrogenetic grids for metacarbonate rocks-Pressure-temperature phase-diagram projection for mixed-volatile systems *Contrib. Mineral. Petrol.*, *108*(1–2), 93–105.

Davies, J. H. (1999), The role of hydraulic fractures in generating intermediate depth earthquakes and subduction zone magmatism, *Nature*, *398*, 142–145.

Deal, M. M., and G. Nolet (1999), Slab temperature and thickness from seismic tomography: 2. Izu-Bonin, Japan, and Kuril subduction zones, *J. Geophys. Res.*, *104*(B12), 28,803–28,812.

Faccenna, C., L. Jolivet, C. Piromallo, and A. Morelli (2003), Subduction and the depth of convection in the Mediterranean mantle, *J. Geophys. Res.*, *108*(B2), 2099, doi:10.1029/2001JB001690.

Gautier, P., J.-P. Brun, R. M. D. Sokoutis, J. Martinod, and L. Jolivet (1999), Timing, kinematics and cause of Aegean extension: A scenario based on a comparison with simple analogue experiments, *Tectonophysics*, *315*(1–4), 31–72.

Gerya, T. V., and D. A. Yuen (2003a), Rayleigh-Taylor instabilities from hydration and melting propel “cold plumes” at subduction zones, *Earth Planet. Sci. Lett.*, *212*, 47–62.

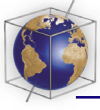
Gerya, T. V., and D. A. Yuen (2003b), Characteristics-based marker-in-cell method with conservative finite-differences schemes for modeling geological flows with strongly variable transport properties, *Phys. Earth Planet. Inter.*, *140*(4), 293–318.

Gerya, T. V., L. L. Perchuk, D. D. Van Reenen, and C. A. Smit (2000), Two-dimensional numerical modeling of pressure-temperature-time paths for the exhumation of some granulite facies terrains in the Precambrian, *J. Geodyn.*, *30*(1–2), 17–35.

Gerya, T. V., L. L. Perchuk, W. V. Maresch, A. P. Willner, D. D. Van Reenen, and C. A. Smit (2002), Thermal regime and gravitational instability of multi-layered continental crust: Implications for the buoyant exhumation of high-grade metamorphic rocks, *Eur. J. Mineral.*, *14*(4), 687–699.

Gerya, T. V., D. A. Yuen, and W. V. Maresch (2004a), Thermomechanical modeling of slab detachment, *Earth Planet. Sci. Lett.*, *226*, 101–116.

Gerya, T. V., R. Uken, J. Reinhardt, M. K. Watkeys, W. V. Maresch, and B. M. Clarke (2004b), “Cold” domes and diapirs triggered by the Bushveld magmatic event: Insight from 2-D numerical modeling, in *Gneiss Domes in Orogeny*,



- edited by D. Whitney, C. Teysier, and C. S. Siddoway, *Spec. Pap. Geol. Soc. Am.*, 380, 117–127.
- Gerya, T. V., D. A. Yuen, and E. O. D. Sevre (2004c), Dynamical causes for incipient magma chambers above slabs, *Geology*, 32(1), 89–92.
- Gerya, T. V., J. A. D. Connolly, D. A. Yuen, W. Gorczyk, and A. M. Capel (2006), Seismic implications of mantle wedge plumes, *Phys. Earth Planet. Inter.*, in press.
- Ghiorso, M. S., M. M. Hirschmann, P. W. Reiners, and V. C. Kress, III (2002), The pMELTS: A revision of MELTS for improved calculation of phase relations and major element partitioning related to partial melting of the mantle to 3 GPa, *Geochem. Geophys. Geosyst.*, 3(5), 1030, doi:10.1029/2001GC000217.
- Hart, S. R., and A. Zindler (1986), In search of a bulk-Earth composition, *Chem. Geol.*, 57(3–4), 247–267.
- Hawkins, J. H., S. H. Bloomer, C. A. Evans, and J. T. Melchior (1984), Evolution of intra-oceanic arc trench system, *Tectonophysics*, 102, 175–205.
- Holland, T., and R. Powell (1996), Thermodynamics of order-disorder in minerals. 2. Symmetric formalism applied to solid solutions, *Am. Mineral.*, 81(11–12), 1425–1437.
- Holland, T. J. B., and R. Powell (1998), An internally consistent thermodynamic data set for phases of petrological interest, *J. Metamorph. Geol.*, 16(3), 309–343.
- Holland, T., J. Baker, and R. Powell (1998), Mixing properties and activity-composition relationships of chlorites in the system MgO-FeO-Al₂O₃-SiO₂-H₂O, *Eur. J. Mineral.*, 10, 395–406.
- Honda, S., and M. Saito (2003), Small-scale convection under the back-arc occurring in the low viscosity wedge, *Earth Planet. Sci. Lett.*, 216(4), 703–715.
- Honda, S., M. Saito, and T. Nakakuki (2002), Possible existence of small-scale convection under the back arc, *Geophys. Res. Lett.*, 29(21), 2043, doi:10.1029/2002GL015853.
- Jolivet, L., and C. Faccenna (2000), Mediterranean extension and the African-Eurasia collision, *Tectonics*, 19, 1095–1106.
- Jolivet, L., and M. Patriat (1999), Ductile extension and the formation of the Aegean Sea, in *The Mediterranean Basins: Tertiary Extension Within the Alpine Orogen*, edited by B. Durand et al., *Geol. Soc. Spec. Publ.*, 156, 427–456.
- Kaus, B. J. P., and Y. Y. Podladchikov (2001), Forward and reverse modeling of the three-dimensional Rayleigh-Taylor instability, *Geophys. Res. Lett.*, 28(6), 1095–1098.
- Kerrick, D. M., and J. A. D. Connolly (1998), Subduction of ophiocarbonates and recycling of CO₂ and H₂O, *Geology*, 26, 375–378.
- Kerrick, D. M., and J. A. D. Connolly (2001a), Metamorphic devolatilization of subducted mid-ocean ridge metabasalts: Implications for seismicity, arc magmatism and volatile recycling, *Earth Planet. Sci. Lett.*, 189, 19–29.
- Kerrick, D. M., and J. A. D. Connolly (2001b), Metamorphic devolatilization of subducted marine sediments and the transport of volatiles into the Earth's mantle, *Nature*, 411, 293–296.
- Lister, G. S., G. A. Banga, and A. Feenstra (1984), Metamorphic core complexes of the Cordilleran type in the Cyclades, Aegean Sea, *Geology*, 12, 221–225.
- Manea, V. C., M. Manea, V. Kostoglodov, and G. Sewell (2005), Thermo-mechanical model of the mantle wedge in central Mexican subduction zone and a blob tracing approach for the magma transport, *Phys. Earth Planet. Inter.*, 149(1–2), 165–186.
- Martelet, G., P. Calcagno, C. Gumiaux, C. Truffert, A. Bitri, D. Gapais, and J. P. Brun (2004), Integrated 3D geophysical and geological modelling of the Hercynian Suture Zone in the Champtoceaux area (south Brittany, France), *Tectonophysics*, 382, 117–128.
- Newton, R. C., T. V. Charlu, and O. J. Kleppa (1980), Thermochemistry of the high structural state plagioclases, *Geochem. Cosmochim. Acta*, 44, 933–941.
- Peacock, S. M., P. E. van Keken, S. D. Holloway, B. R. Hacker, G. A. Abers, and R. L. Fergason (2005), Thermal structure of the Costa Rica-Nicaragua subduction zone, *Phys. Earth Planet. Inter.*, 149, 187–200.
- Pinkerton, H., and R. J. Stevenson (1992), Methods of determining the rheological properties of magmas at subliquidus temperatures, *J. Volcanol. Geotherm. Res.*, 53, 47–66.
- Plank, T., and C. H. Langmuir (1998), The chemical composition of subducting sediment and its consequences for the crust and mantle, *Chem. Geol.*, 145(3–4), 325–394.
- Poli, S., and M. W. Schmidt (2002), Petrology of subducted slabs, *Annu. Rev. Earth Planet. Sci.*, 30, 207–235.
- Ponko, S. C., and S. M. Peacock (1995), Thermal modeling of the southern Alaska subduction zone: Insight into the petrology of the subducting slab and overlying mantle wedge, *J. Geophys. Res.*, 100(B11), 22,117–22,128.
- Powell, R., and T. Holland (1999), Relating formulations of the thermodynamics of mineral solid solutions: Activity modeling of pyroxenes, amphiboles, and micas, *Am. Mineral.*, 84(1–2), 1–14.
- Ranalli, G. (1995), *Rheology of the Earth*, 413 pp., CRC Press, Boca Raton, Fla.
- Regenauer-Lieb, K., D. A. Yuen, and J. Branlund (2001), The initiation of subduction: Criticality by addition of water?, *Science*, 294(5542), 578–580.
- Rudolph, M. L., T. V. Gerya, and D. A. Yuen (2005), Challenges in the visualization of a mantle dynamics simulation using one billion tracers, *Comput. Fluid Solid Mech.*, in press.
- Rupke, L. H., J. P. Morgan, L. H. M. Hort, and J. A. D. Connolly (2004), Serpentine and the subduction zone water cycle, *Earth Planet. Sci. Lett.*, 223(1–2), 17–34.
- Schmidt, M. W., and S. Poli (1998), Experimentally based water budgets for dehydrating slabs and consequences for arc magma generation, *Earth Planet. Sci. Lett.*, 163(1–4), 361–379.
- Schurr, B. (2001), Seismic structure of the Central Andean subduction zone from local earthquake data, *Sci. Tech. Rep. STR01/01*, GeoForschungsZentrum Potsdam, Potsdam, Germany.
- Schurr, B., G. Asch, A. Rietbrock, R. Trumbull, and Ch. Haberland (2003), Complex patterns of fluid and melt transport in the central Andean Subduction zone revealed by attenuation tomography, *Earth Planet. Sci. Lett.*, 215(1–2), 105–119.
- Staudigel, H., S. R. Hart, H-U. Schmincke, and B. M. Smith (1989), Cretaceous ocean crust at DSDP sites 417–418: Carbon uptake from weathering versus loss by magmatic outgassing, *Geochim. Cosmochim. Acta*, 53, 3091–3094.
- Stern, R. J. (2002), Subduction zones, *Rev. Geophys.*, 40(4), 1012, doi:10.1029/2001RG000108.
- Tamura, Y. (1994), Genesis of island-arc magmas by mantle-derived bimodal magmatism-Evidence from the Shirahama Group, Japan, *J. Petrol.*, 35(3), 619–645.
- Tamura, Y., Y. Tatsumi, D. Zhao, Y. Kido, and H. Shukuno (2002), Hot fingers in the mantle wedge: New insights into magma genesis in subduction zones, *Earth Planet. Sci. Lett.*, 197(1–2), 105–116.
- Thompson, A. B., and J. A. D. Connolly (1995), Melting of the continental crust: Some thermal and petrological constraints on anatexis in continental collision zones and other tectonic settings, *J. Geophys. Res.*, 100(B8), 15,565–15,580.

- Thompson, A. B., and G. L. Hovis (1979), Entropy of mixing in Sanidine, *Am. Mineral.*, *64*(1–2), 57–65.
- Uyeda, S., and H. Kanamori (1979), Back-arc opening and the mode of subduction, *J. Geophys. Res.*, *84*, 1049–1060.
- van der Meijde, M., S. van der Lee, and D. Giardini (2005), Seismic discontinuities in the Mediterranean mantle, *Phys. Earth Planet. Inter.*, *148*, 233–250.
- van Hunen, J., A. P. Van Den Berg, and N. J. Vlaar (2000), A thermo-mechanical model of horizontal subduction below an overriding plate, *Earth Planet. Sci. Lett.*, *182*(2), 157–169.
- Vasilyev, O. V., T. V. Gerya, and D. A. Yuen (2004), The application of multidimensional wavelets to unveiling multi-phase diagrams and in situ physical properties of rocks, *Earth Planet. Sci. Lett.*, *223*, 49–64.
- Wei, C. J., and R. Powell (2003), Phase relations in high-pressure metapelites in the system KFMASH (K_2O - FeO - MgO - Al_2O_3 - SiO_2 - H_2O) with application to natural rocks, *Contrib. Mineral. Petrol.*, *145*(3), 301–315.
- White, R. W., R. Powell, and G. N. Phillips (2003), A mineral equilibria study of the hydrothermal alteration in mafic greenschist facies rocks at Kalgoorlie, Western Australia, *J. Metamorph. Geol.*, *21*(5), 455–468.
- Willner, A. P., E. Sebazungu, T. V. Gerya, W. V. Maresch, and A. Krohe (2002), Numerical modeling of PT paths related to rapid exhumation of high-pressure rocks from the crustal root in the Variscan Erzgebirge Dome (Saxony/Germany), *J. Geodyn.*, *33*, 281–314.
- Willner, A. P., J. Glodny, T. V. Gerya, E. Godoy, and H. J. Massonne (2004), A counterclockwise PTt path of high-pressure/low-temperature rocks from the Coastal Cordillera accretionary complex of south-central Chile: Constraints for the earliest stage of subduction mass flow, *Lithos*, *75*, 283–310.
- Wortel, M. J. R., and W. Spakman (2000), Subduction and slab detachment in the Mediterranean-Carpathian region, *Science*, *290*(5498), 1910–1917.
- Zhang, H. J., C. H. Thurber, D. Shelly, S. Ide, G. C. Beroza, and A. Hasegawa (2004), High-resolution subducting-slab structure beneath northern Honshu, Japan, revealed by double-difference tomography, *Geology*, *32*(4), 361–364.
- Zhao, D. P. (2004), Global tomographic images of mantle plumes and subducting slabs: insight into deep Earth dynamics, *Phys. Earth Planet. Inter.*, *146*(1–2), 3–34.